J. Solid Mech. 2026; 18(01): 35-58

Journal of Solid Mechanics

https://doi.org/10.57647/jsm.2026.1801.03

Research Article

Vibration Analysis of a Sandwich Microbeam with Functionally Graded Porous Core and CNT Face Sheets, Considering Surface Effects

Arezo Havazadeh[1], Ali Ghorbanpour Arani*[1], Hamed Khani Arani[2]

[1]*Department of Solid Mechanics, Faculty of Mechanical Engineering, University of Kashan, Kashan, Iran*
[2]*Faculty of Mechanical Engineering, K N Toosi University of Technology, Tehran, Iran*

***Corresponding author:** aghorban@kashanu.ac.ir

Article History:

Received:
09 February 2026
Revised:
12 March 2026
Accepted:
20 March 2026
Published in Issue:
31 March 2026

Abstract

In this research, the vibration behavior of a sandwich microbeam with a graded porous core and carbon nanotube (CNT)-reinforced surfaces resting on a Visco-Pasternak foundation and taking surface effects into account is investigated. Moreover, to achieve accurate results, surface phenomena such as surface elasticity and residual stresses are incorporated by using the Mori-Tanaka homogenization method and Gurtin-Murdoch model, while the porous core's properties are characterized by a symmetric porosity distribution model. The governing equations are derived based on the third-order shear deformation theory (Reddy beam theory) and Hamilton's principle. These equations are solved using the generalized differential quadrature method, accompanied by a detailed numerical study employing the modified couple stress theory (MCST). A parametric study is presented to investigate the impact of various characteristics, including the geometric properties, porosity and distribution pattern of pores, mass fraction, type and distribution pattern of CNTs, material length scale parameter, foundation parameters, and boundary conditions on the natural frequency of a sandwich microbeam. Results quantitatively show that 1% CNT mass fraction increase natural frequencies by 5-12% and damping by 10%, with surface effects adding up to 15% frequency enhancement and viscoelastic foundation improving the damping by 20%. The presented results can be used in the optimal design and analysis of the lightweight and robust structures in aerospace and advanced engineering applications.

Keywords: Vibration; Sandwich micro beam; Porous; Carbon nanotube; Surface effect

Cite this article: Havazadeh, A., Ghorbanpour Arani, A., Khani Arani, H., (2026). Vibration Analysis of a Sandwich Microbeam with Functionally Graded Porous Core and CNT Face Sheets, Considering Surface Effects, *Journal of Solid Mechanics,* 18(01): 35-58.
https://doi.org/10.57647/jsm.2026.1801.03

1. Introduction

In recent years, sandwich structures at nano/micro scales have attracted a huge attention in biomechanics, and the investigation of the mechanical behavior of these types of structures is an essential endeavor to design small-scaled devices. On the one hand, functionally graded porous (FGP) materials are porous structures with a porosity gradient distributed over volume. Porous materials, characterized by the presence of micropores, exhibit very low density, which significantly reduces the overall mass of structures incorporating them. Moreover, their advantageous properties extend beyond low density, including high recyclability, effective sound insulation, substantial energy absorption capacity, and extremely low thermal conductivity near absolute zero temperature. On the other hand, carbon nanotubes (CNTs) are recognized as suitable reinforcement materials for composites, due to their exceptional mechanical properties, including high tensile strength, high elastic modulus, and low density, which provide significant improvements in strength, stiffness, and impact resistance.

Notably, FGP and CNTs have attracted considerable attention due to their unique properties, and these characteristics have led to numerous applications in various engineering fields such as aerospace, automotive, civil engineering, electronics, energy storage, sensors, and biomechanics [1-4]. The following is a review of previous works. Chen et al. [5-7] extended the problem of static bending, elastic buckling, free vibration, and forced vibration, for FGP beams with the consideration of shear effects through an analytical analysis framework.

Then, Chen et al. [8] reviewed the recent research advances for FGP structures by centring on the adopted mechanical analysis approaches, the obtained findings, and the application opportunities. An analytical approach for free vibration and static buckling analyses of FGP beams with nano-graphene platelet reinforcements was investigated by Kitipornchai et al. [9]. Free and forced vibration analyses of FGP beam-type structures based on the finite element method and both Euler Bernoulli and Timoshenko beam theories proposed by Wu et al. [10]. Enayat et al. [4] focused on the bending, buckling, and vibration analyses of FGP nanobeams resting on a Pasternak foundation incorporating surface effects based on Euler-Bernoulli, Timoshenko, and Reddy's third-order shear deformation beam theories. They revealed that the minimum value of the static deflection and maximum values of critical buckling load and fundamental frequency can be achieved using symmetric distribution pattern of pores. Alphonse et al. [11] presented the effect of the mechanical behavior of sandwich structures with varying core material. Their results indicated that the mechanical properties vary significantly with different core and base metal combinations, influencing different applications. Safari et al. [12] investigated the free vibration behavior of a sandwich electro-magneto-thermal Timoshenko beam composed of a porous core and composite faces reinforced with graphene sheets, within a thermal environment. Their findings revealed that geometric characteristics and material variations substantially affect the natural frequency of the sandwich beam, and that incorporating graphene sheets and piezoelectric-magneto-electric layers can markedly improve the vibration performance of microstructures. Eftekhari and Toghraie [13] examined the vibration behavior and stability of sandwich-structured microbeams based on higher-order strain gradient theories. They analyzed the effects of small-scale size, surface properties, and other parameters on beam vibrations. Ruocco and Reddy [14] conducted a comparative analysis of the Reddy, Timoshenko, and Bernoulli beam models, highlighting the limitations of beam theories in engineering applications. They found that the Reddy beam model more accurately predicts stress fields, whereas simpler models like Euler-Bernoulli and Timoshenko are suitable for displacement analysis but less accurate for stress estimation. The dynamic behavior of a sandwich beam with a porous core and carbon nanotube-reinforced polymer facesheets under moving mass loads was analyzed by Biglari et al. [15]. Results showed that increasing core porosity elevates natural frequencies and critical speeds, as mass reduction outweighs stiffness reduction. Asgari et al. [16] developed static bending, free vibration, and buckling responses of a sandwich beam composed of a five-layer considering a Honeycomb core and CNT- reinforced composite with shape memory alloy particles, using sinusoidal shear deformation beam theory. Their results revealed that increasing CNT volume fraction reduces beam displacement by 30%. Khoshgoftar et al. [17] reported dynamic properties of composite nanobeams with the top and bottom face sheets incorporate CNTs, distributed either uniformly or in a functionally graded manner, and hybrid cellular cores using nonlocal Eringen elasticity and modified shear deformation theories. They found that functional CNT distribution enhances natural frequencies. Shahidi and Mohammadimehr [18] analyzed the free vibration of rotating sandwich beams with an aluminum foam core and carbon nanotube-reinforced composite face sheets subjected to thermal and moisture fields. The Euler-Bernoulli beam theory and the Generalized Differential Quadrature Method (GDQM) were employed. The results indicate that the presence of delamination, the type of contact in the debonded region, as well as variations in temperature, moisture, and rotational speed, have a significant effect on the natural frequencies. Rostami and Mohammadimehr [19] presented an analytical approach for vibration control of a rotating sandwich cylindrical shell integrated with a porous core, carbon nanotube-reinforced composite face sheets, and magneto-electro-elastic functionally graded layers. Mohammadimehr [20] investigated the vibration behavior of a Timoshenko sandwich beam with a porous core and functionally graded material face sheets. The results showed that increasing the nonlocal stress parameter reduces the natural frequency, whereas the nonlocal strain parameter has the opposite effect.

The foregoing literature survey reflects some of the most relevant and correct articles in the field of the subject of the current research. For the first time, a vibration behavior of the sandwich micro beam with FGP core and CNT layers on a Visco-Pasternak foundation by considering surface effects and using the Mori-Tanaka homogenization and the Gurtin-Murdoch models is presented.

The practical applications of this study include the optimal design of lightweight, high-stiffness microstructures in aerospace (e.g., satellite components, vibration isolators), biomechanics (e.g., micro-actuators, bio-sensors), and advanced engineering (e.g., MEMS/NEMS devices, energy harvesters).

This work holds significant importance by quantifying the synergistic effects of porosity, CNTs, and surface phenomena revealing up to 15% frequency enhancement from surface effects and 20% damping improvement from viscoelastic foundation which guides the development of robust, porous-CNT sandwich structures for high-frequency, low-mass applications under micro-scale constraints.

The novelty of this work lies in the simultaneous consideration of porosity, CNT agglomeration, visco-Pasternak foundation, with Mori-Tanaka/Gurtin-Murdoch surface effects and size effects in evaluating the vibrational of the sandwich microbeams. Finally, the present work aims to provide a comprehensive and innovative analysis of sandwich beam structures.

2. Structural definitions

Let us consider the sandwich micro beam with FGP core and CNT layers on a Visco-Pasternak foundation that is shown in Figure 1.

Based on a Cartesian coordinate system, the symbols L and b denote the length and width of the beam, containing a porous core with a thickness h_c, whereas the two polymer-based facings are reinforced with CNTs with equal thickness h_f.

For modeling and analysis of this structure, there are several assumptions such as:

• No slip or delamination occurs between the layers of the microbeam (perfect bonding).

• The microbeam is fully surrounded by the foundation; in other words, the contact between the microbeam and the foundation is complete and does not break during oscillations. If this assumption is not considered, the force exerted by the foundation on the microbeam would be nonlinear and complex.

• The amplitude of the microbeam oscillations is small compared to its dimensions, to the extent that the equations can be analyzed in the linear vibration domain (small amplitude assumption).

• The FG porous core materials follow uniform porosity distribution patterns (UU, VV, XX, etc.), with CNT-reinforced face sheets assumed isotropic/orthotropic.

• Surface effects are incorporated via the Gurtin-Murdoch model, and displacement fields are based on TSDT. To analyse this structure, the stress-strain relations are written for every layer and strain, and kinetic energies of each layer are separately calculated; therefore, the energy of the system is the sum of energy in each layer.

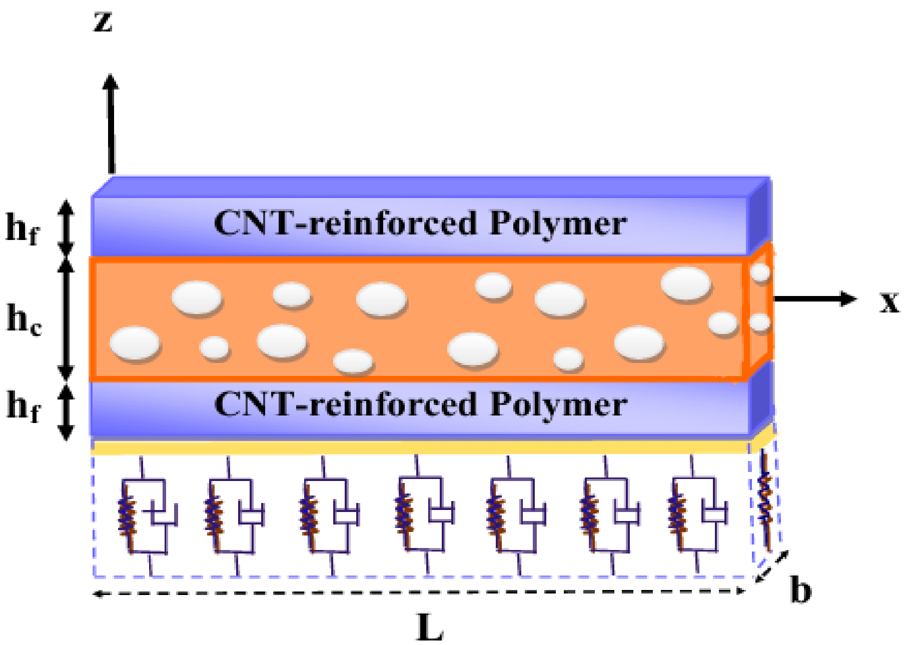

Figure 1. The geometry of an FG porous-nanocomposite sandwich microbeam

10.57647/jsm.2026.1801.03

3. Mathematical derivations

3.1. Porous core modeling

In this study, as illustrated in Figure 2, three different pore distribution patterns are considered: Uniform distribution (U), Symmetric distribution type 1 (SI), and Symmetric distribution type 2 (SII). For the U pattern, the prose size in the core is constant, and the prose distribution pattern is uniform; so, the core is homogeneous, and this pattern is defined based on Eq. (1). For the SI and SII, the size changes along the thickness of the microbeam core, so the core is inhomogeneous. In the SI pattern, the pores near the mid-surface (z = 0) are larger, and the size of the pores decreases as one move toward the lower and upper surfaces of the core (z = $\pm 0.5h_c$). While, SII pattern exhibits a completely opposite trend, where the pores near the lower and upper surfaces of the core are larger, and the size of the pores decreases as one move toward the mid-surface. These distribution patterns are considered based on Eqs. (2) and (3), respectively [21-24].

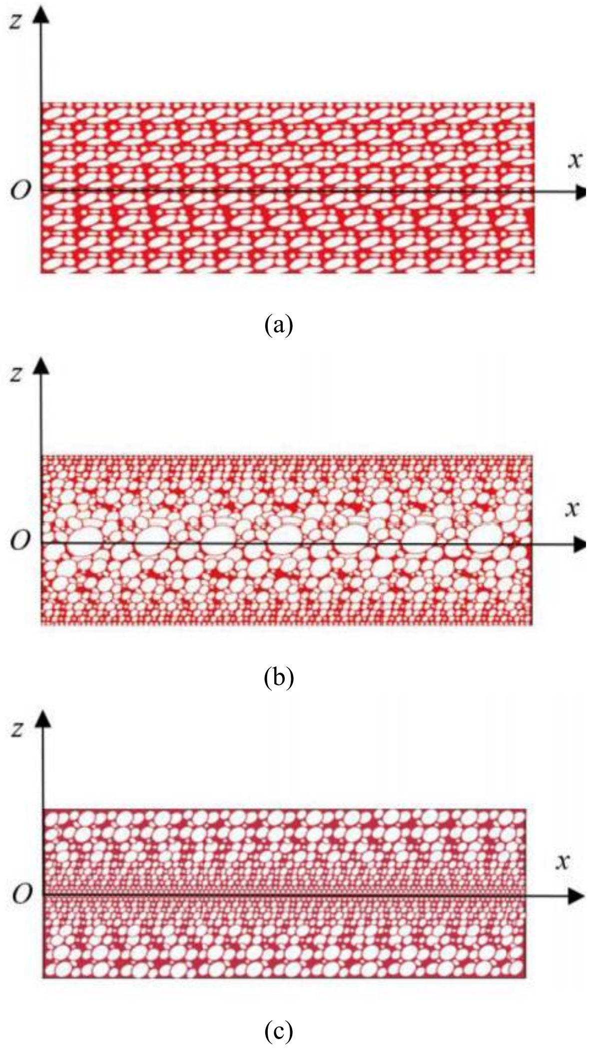

Figure 2. Holes distribution pattern in the porous core: a) U, b) SI, c) SII [23]

$$U: f(z) = 1 - e_0\eta$$
$$\eta = \frac{1}{e_0} - \frac{1}{e_0}\left(\frac{2}{\pi}\sqrt{1-e_0} - \frac{2}{\pi} + 1\right)^2 \tag{1}$$

$$SI: f(z) = 1 - e_1 \cos\left(\frac{\pi z}{h_c}\right) \tag{2}$$

$$SII: f(z) = 1 - e_2 \cos\left(\frac{\pi z}{2h_c} + \frac{\pi}{4}\right) \tag{3}$$

In which $f(z)$ is used to denote different distributions, and $e_0, e_1, e_2$are the coefficients represent the degree of porosity. For example, when the core is not porous these coefficients are $e_0 = e_1 = e_2 = 0$ and an increase in these coefficients corresponds to larger pore sizes. The variation of the core's modulus of elasticity according to these pore distribution patterns is expressed as follows [23]:

$$E_c = E_m f(z) \tag{4}$$

In which, E_c is the elastic modulus of the porosity core and E_0 is the elastic modulus of the core when it is not porous. Also, in porous materials, the following dependency between date elastic modulus and density ρ_c holds [25].

$$\frac{E_c}{E_0} = \left(\frac{\rho_c}{\rho_0}\right)^{2.73} = f(z) \tag{5}$$

Furthermore, assuming isotropic behavior for this class of materials, the shear modulus can be determined using the following relation [26]:

$$G(z) = \frac{E_c(z)}{2(1+v)} \tag{6}$$

3.2. Carbon nanotube face sheets

Microbeam face sheets are designed from polymers reinforced with CNTs. In this analysis, it is assumed that the thicknesses of both layers are equal. As shown in Figure 3, five different patterns of carbon nanotube distribution are investigated: uniform distribution (U) and four non-uniform graded patterns labeled A, V, O, and X. In the uniform distribution pattern (U), the volume fraction of carbon nanotubes remains constant throughout the entire structure, resulting in a homogeneous material. In contrast, the graded patterns A and V feature a linear variation of the volume fraction, ranging from zero to twice the average volume fraction, leading to a heterogeneous structure with gradual changes. The O pattern increases the concentration of nanotubes at the center of the material, whereas the X pattern includes two intersecting regions with a high density of nanotubes, potentially creating zones with enhanced strength and unique properties [27, 28].

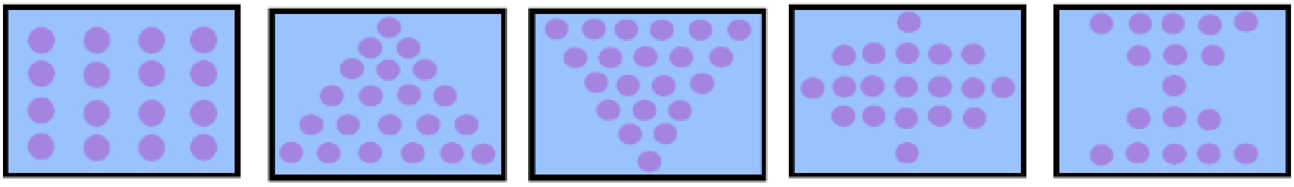

Figure 3. Distribution patterns of CNTs in the face sheets

The volume fraction distribution of carbon nanotubes in the bottom layer$(-0.5h \leq z \leq 0.5\,h_c)$, denoted by the subscript b, and the top layer $(-0.5h_c \leq z \leq 0.5h)$, denoted by the subscript t can be expressed using the following relations, depending on the chosen pattern [25].

$$U{:}\, F_r^b(z) = F_r^*$$
$$A{:}\to F_r^b(z) = F_r^*\left[1+\frac{2}{h_f}\left(z+\frac{h_c+h_f}{2}\right)\right]$$
$$V{:}\to F_r^b(z) = F_r^*\left[1-\frac{2}{h_f}\left(z+\frac{h_c+h_f}{2}\right)\right] \quad (7)$$
$$X{:}\to F_r^b(z) = \frac{4F_r^*}{h_f}\left|z+\frac{h_c+h_f}{2}\right|$$
$$O{:}\to F_r^b(z) = 2F_r^*\left[1-\frac{2}{h_f}\left|z+\frac{h_c+h_f}{2}\right|\right]$$

$$U{:}\, F_r^t(z) = F_r^*$$
$$A{:}\to F_r^t(z) = F_r^*\left[1+\frac{2}{h_f}\left(z-\frac{h_c+h_f}{2}\right)\right]$$
$$V{:}\to F_r^b(z) = F_r^*\left[1-\frac{2}{h_f}\left(z-\frac{h_c+h_f}{2}\right)\right] \quad (8)$$
$$X{:}\to F_r^t(z) = \frac{4F_r^*}{h_f}\left|z-\frac{h_c+h_f}{2}\right|$$
$$O{:}\to F_r^t(z) = 2F_r^*\left[1-\frac{2}{h_f}\left|z-\frac{h_c+h_f}{2}\right|\right]$$

where F_r is the average volume fraction of carbon nanotubes, which is assumed to be a constant value in each period. Also, the average volume fraction of carbon nanotubes can be calculated based on the mass fraction of nanotubes:

$$F_r^* = \frac{1}{1+\frac{\rho_r}{\rho_m}\left(\frac{1}{w_r}-1\right)} \quad (9)$$

In which w_r is the mass fraction of nanotubes, ρ_m is the properties of the polymer matrix, and ρ_r is the density of carbon nanotubes. In addition, the volume fraction of the polymer matrix on microbeam surfaces can be determined using the following equation [27, 28].

$$F_m = 1 - F_r \qquad i = b,t \quad (10)$$

It should be noted that the changes in volume fraction distribution patterns are adjusted such that the average volume fraction and, consequently, the mass fraction of carbon nanotubes remain equal in all three cases. The orientation and packing density of carbon nanotubes do not affect the overall density of the nanocomposite structure; therefore, the rule of mixtures can be applied to calculate the density as follows [29]:

$$\rho_i(z) = \rho_m F_m^i(z) + \rho_r F_r^i(z) \qquad i = b,t \quad (11)$$

3.3. Third-order shear deformation theory (TSDT)

In the current research, the displacement field in the microbeam is considered based on the TSDT (Reddy beam theory). This theory ensures the transverse shear stresses vanish at the top and bottom surfaces of the beam, thereby satisfying the essential physical boundary conditions. Because the higher-order terms in Reddy's theory naturally capture the parabolic-like shear stress distribution, the shear correction factor is no longer required to adjust the shear energy. TSDT extends the first-order shear deformation theory (FSDT) by assuming that:

- Shear strain and stress are not constant through the beam thickness, where for a moderately thick beam, TSDT leads to better results.
- The strain equations do not need a shear correction factor.
- The displacement field accommodates a quadratic variation of the transverse shear through the thickness and the vanishing of transverse shear stresses on the top and bottom surfaces of the beam.

Then, the displacement field for a beam can be expressed as follows [29, 30]:

$$u(x,z,t) = u(x,t) + [f(z)-z]\frac{\partial w(x,t)}{\partial x}$$
$$-f(z)\Psi(x,t)$$
$$v(x,z,t) = 0 \quad (12)$$
$$w(x,z,t) = w(x,t)$$
$$f(z) = z - \frac{4z^3}{3h^2}$$

10.57647/jsm.2026.1801.03

where u, v and w represent the displacements along the x, y and z axes, respectively. The values of the rotations about these axes are also specified. The variable t denotes time, and h is the thickness of the beam, which may vary for each layer. Based on the strain-displacement relations, the non-zero components of the strain tensor can be calculated using Eq. (13) [31]:

$$\begin{aligned} \varepsilon_{ij} &= \frac{1}{2}(u_{i,j} + u_{j,i}) \\ \varepsilon_{xx} &= \frac{\partial u}{\partial x} + [f(z) - z]\frac{\partial^2 w}{\partial x^2} - f(z)\frac{\partial \Psi}{\partial x} \\ \gamma_{xz} &= g(z)\left(\frac{\partial w}{\partial x} - \Psi\right) \\ g(z) &= \frac{df}{dz} = 1 - \left(\frac{2z}{h}\right)^2 \end{aligned} \tag{13}$$

Also, in accordance with Hooke's law, the stress-strain relationship is given by:

$$\sigma_{xx} = E\varepsilon_{xx}, \qquad \sigma_{xz} = G\gamma_{xz} \tag{14}$$

in which E and G represent the elastic modulus and shear modulus of the material, respectively. To account for surface effects in the analysis of microbeams, the modeling approach considers the microbeam as a main bulk volume surrounded by a thin surface layer, as shown in Figure 4. This surface layer significantly influences the overall behavior of the structure due to its distinct physical and mechanical properties and therefore must be analyzed separately. Based on the surface elasticity theory developed by Gurtin -Murdoch, the shear and normal stress components within this surface layer are rigorously defined as calculated in Eq. (15), enabling a more comprehensive and accurate analysis of surface effects [32].

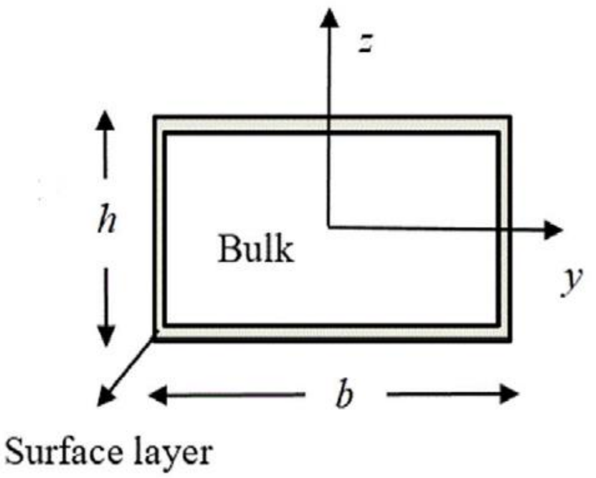

Figure 4. The surface layer in the microbeam [4]

$$\sigma_{xx}^s = E^s\varepsilon_{xx} + \tau^s \qquad \sigma_{xz}^s = \tau^s\frac{\partial w}{\partial x} \tag{15}$$

In this regard, the superscript "s" denotes the surface-related quantities, such that E^s and τ^s represent the surface elastic modulus and the residual surface stress of the microbeam, respectively. In the modified surface texture beam theory, the normal stress component (σ_{zz}) is often neglected.

However, this assumption violates the surface equilibrium conditions defined within the framework of surface elasticity theory.

Therefore, it is necessary to account for the normal stress component, and it is assumed that this normal stress component varies linearly along the thickness direction, ensuring that the surface equilibrium equations are properly satisfied. This approach improves the accuracy of the model and provides a better representation of the actual physical behavior [33].

$$\sigma_{zz} = \frac{2z}{h}\left(\tau^s\frac{\partial^2 w}{\partial x^2} - \rho^s\frac{\partial^2 w}{\partial t^2}\right) \tag{16}$$

where ρ^s is the surface density.

By considering the vertical component of stress in the direction of the microbeam thickness and using Eqs. (15) and (16), Eq. (14) is modified to Eq. (17), and the accuracy of the model in describing the mechanical behavior of the structure is improved [34].

$$\begin{aligned} \sigma_{xx} &= E\varepsilon_{xx} + \upsilon\sigma_{zz} \\ &= E\left\{\frac{\partial u}{\partial x} + [f(z) - z]\frac{\partial^2 w}{\partial x^2} - f(z)\frac{\partial \Psi}{\partial x}\right\} \\ &+ \frac{2\upsilon z}{h}\left(\tau^s\frac{\partial^2 w}{\partial x^2} - \rho^s\frac{\partial^2 w}{\partial t^2}\right) \\ \sigma_{xz} &= Gg(z)\left(\frac{\partial w}{\partial x} - \Psi\right) \end{aligned} \tag{17}$$

4. Equations of motion

The energy method is used to obtain the governing equation in this work; therefore, the strain and kinetic energy are obtained for any layer, and after that layers are summed together. Then, Hamilton's principle gives the governing equations for the dynamic behavior of a structure, along with the associated boundary conditions. Hamilton's principle can be obtained [27]:

$$\int_{t_1}^{t_2} (\delta U + \delta T + \delta W_{n.c.})\, dt = 0 \tag{18}$$

10.57647/jsm.2026.1801.03

in which t_1, t_2 represent an arbitrary time interval, δ denotes the variation operator, U and T correspond to the potential energy and kinetic energy of the microbeam, and $W_{n.c.}$ is the work done by external forces.

4.1. Strain energy based on modified couple stress theory (MCST)

Based on the MSCT, the strain energy density is a function of both strain and gradient of the rotation vector. For linear isotropic elastic materials, the strain energy is expressed as follows [35, 36]:

$$U = \frac{1}{2}\int_V (\sigma_{ij}\varepsilon_{ij} + m_{ij}\chi_{ij})dV \qquad i,j = x,z$$

$$U = \frac{1}{2}\int_V (\sigma_{xx}\varepsilon_{xx} + \sigma_{xz}\varepsilon_{xz} + 2m_{xy}\chi_{xy} \tag{19}$$

$$+2m_{yz}\chi_{yz})dV$$

in which U denotes the strain energy, m_{ij} the components of the deviator section represent the pair stresses, and χ_{ij} the components of the curvature symmetry tensor are given by:

$$m_{ij}(x,y,z) = 2\mu(z)l^2\chi_{ij}$$

$$\mu(z) = \frac{E(z)}{2[1+\upsilon(z)]}$$

$$\chi_{ij} = \frac{1}{2}(\theta_{i,j} + \theta_{j,i}) \tag{20}$$

$$\theta_i = \frac{1}{2}e_{ijk}u_{kj}$$

where l and $\mu(z)$ are the material length scale parameter and Lamé constant, $E(z)$ and $\nu(z)$ are defined as functions of Young's modulus and Poisson's ratio, θ_i represents the components of the rotation vector, and e_{ijk} is the permutation symbol. The components of the curvature symmetry tensor are likewise determined by Eq. (20):

$$\chi_{xy} = \frac{1}{4}\left\{[g(z)-2]\frac{\partial^2 w}{\partial x^2} - g(z)\frac{\partial \Psi}{\partial x}\right\}$$

$$\chi_{yz} = \frac{d(z)}{4}\left\{\frac{\partial w}{\partial x} - \Psi\right\} \tag{21}$$

$$d(z) = \frac{dg}{dz} = -\frac{8z}{h^2}$$

By using Eqs. (19) - (21), the variation in the strain energy is given by:

$$\delta U = \int_0^L \iint_S \left\langle \sigma_{xx}\left\{\frac{\partial \delta u}{\partial x} + [f(z)-z]\frac{\partial^2 \delta w}{\partial x^2}\right.\right.$$

$$\left.\left. - f(z)\frac{\partial \delta\Psi}{\partial x}\right\} + \sigma_{xz}g(z)\left(\frac{\partial \delta w}{\partial x} - \delta\Psi\right)\right\rangle$$

$$+\left\langle \frac{m_{xy}}{2}\left\{[g(z)-2]\frac{\partial^2 \delta w}{\partial x^2} - g(z)\frac{\partial \delta\Psi}{\partial x}\right\}\right. \tag{22}$$

$$\left. + \frac{m_{yz}d(z)}{2}\left(\frac{\partial \delta w}{\partial x} - \delta\Psi\right)\right\rangle dSdX$$

For ease of solution, the force and moment resultants are defined as follow:

$$\begin{Bmatrix} N_{xx} \\ M_{xx} \\ P_{xx} \end{Bmatrix} = \iint_S \sigma_{xx}(1, z, f(z))dS$$

$$Q_{xz} = \iint_S \sigma_{xz}\, g(z)dS \tag{23}$$

Also, due to the difference in the nature of stress in the bulk and the microbeam surface, Eq. (23) should be presented as fallow:

$$\begin{Bmatrix} N_{xx} \\ M_{xx} \\ P_{xx} \end{Bmatrix} = \iint_A \sigma_{xx}(1, z, f(z))dA$$

$$+\oint \sigma_{xx}^s(1, z, f(z))dS \tag{24}$$

$$Q_{xz} = \iint_A \sigma_{xz}\, g(z)dA + \oint \sigma_{xz}^s g(z)ds$$

Furthermore, the components of the pair stress deformation section can be written as follows:

$$\begin{Bmatrix} p_{ij} \\ q_{ij} \\ r_{ij} \end{Bmatrix} = \iint_s m_{ij}(1, g(z), d(z))ds \tag{25}$$

$$i,j = xy, yz$$

By substituting Eqs. (23)-(25) into Eq. (22), the variation in the strain energy is obtained:

$$\delta U = \int_0^L \left[N_{xx}\frac{\partial \delta u}{\partial x} + (P_{xx} - M_{xx})\frac{\partial^2 \delta w}{\partial x^2}\right.$$

$$\left. - P_{xx}\frac{\partial \delta\Psi}{\partial x} + Q_{xz}\left(\frac{\partial \delta w}{\partial x} - \delta\Psi\right)\right] +$$

$$\left[\left(\frac{q_{xy}}{2} - p_{xy}\right)\frac{\partial^2 \delta w}{\partial x^2} - \frac{q_{xy}}{2}\frac{\partial \delta\Psi}{\partial x}\right. \tag{26}$$

$$\left. + \frac{r_{yz}}{2}\left(\frac{\partial \delta w}{\partial x} - \delta\Psi\right)\right] dx$$

where in the above equation:

$$N_{xx} = b\left(B_0\frac{\partial u}{\partial x} + C_1\frac{\partial^2 w}{\partial x^2} - B_3\frac{\partial \Psi}{\partial x} - b_1\frac{\partial^2 w}{\partial t^2} + h_0\right)$$

$$M_{xx} = b\left(B_1\frac{\partial u}{\partial x} + C_2\frac{\partial^2 w}{\partial x^2} - B_5\frac{\partial \Psi}{\partial x} - b_2\frac{\partial^2 w}{\partial t^2} + h_1\right)$$

$$P_{xx} = b\left(B_3\frac{\partial u}{\partial x} + C_3\frac{\partial^2 w}{\partial x^2} - B_4\frac{\partial \Psi}{\partial x} - b_5\frac{\partial^2 w}{\partial t^2} + h_3\right) \tag{27}$$

$$Q_{xz} = b\left(B_6\frac{\partial w}{\partial x} - A_6\Psi\right)$$

$$p_{xy} = b\left[l^2(m_1 - 2m_0)\frac{\partial^2 w}{\partial x^2} - l^2 m_1\frac{\partial \Psi}{\partial x}\right]$$

$$q_{xy} = b\left[l^2(m_2 - 2m_1)\frac{\partial^2 w}{\partial x^2} - l^2 m_2\frac{\partial \Psi}{\partial x}\right]$$

$$r_{xy} = bl^2 m_3\left(\frac{\partial w}{\partial x} - \Psi\right)$$

in which:

$$C_1 = B_3 - B_1 + a_1$$

$$C_2 = B_5 - B_2 + a_2$$

$$C_3 = B_4 - B_5 + a_5$$

$$B_i = A_i - C_i \qquad j = 0,1,2,3,4,5$$

$$B_6 = A_6 - h_6$$

$$\begin{Bmatrix} A_0 \\ A_1 \\ A_2 \\ A_3 \\ A_4 \\ A_5 \end{Bmatrix} = \int_{-h/2}^{h/2} E(z)\begin{Bmatrix} 1 \\ z \\ z^2 \\ f(z) \\ f^2(z) \\ zf \end{Bmatrix} dz \tag{28}$$

$$A_6 = \int_{-h/2}^{h/2} G(z) g^2(z) dz.$$

$$\begin{Bmatrix} m_0 \\ m_1 \\ m_2 \\ m_3 \end{Bmatrix} = \frac{l^2}{2}\int_{-h/2}^{h/2} G(z)\begin{Bmatrix} 1 \\ g(z) \\ g^2(z) \\ d^2(z) \end{Bmatrix} dz$$

$$(a_1, a_2, a_3) = \frac{2\upsilon}{h}\int_{-h/2}^{h/2} \tau^s(z)\left(z, z^2, zf(z)\right) dz$$

$$(b_1, b_2, b_5) = \frac{2\upsilon}{h}\int_{-h/2}^{h/2} \rho^s(z)\left(z, z^2, zf(z)\right) dz$$

$$\begin{Bmatrix} C_0 \\ C_1 \\ C_2 \\ C_3 \\ C_4 \\ C_5 \end{Bmatrix} = \oint E^s(x)\begin{Bmatrix} 1 \\ z \\ z^2 \\ f(z) \\ f^2(z) \\ zf(z) \end{Bmatrix} ds$$

$$\begin{Bmatrix} h_0 \\ h_1 \\ h_3 \\ h_6 \end{Bmatrix} = \frac{1}{b}\oint_{\Gamma} \tau^s(z)\begin{Bmatrix} 1 \\ z \\ f(z) \\ g(z) \end{Bmatrix} ds$$

4.2. Kinetic energy

The kinetic energy of the microbeam can be stated as [27]:

$$T = \frac{1}{2}\int_0^L \iint_S \rho(z)\left[\left(\frac{\partial u}{\partial t}\right)^2 + \left(\frac{\partial w}{\partial t}\right)^2\right] dS dx \tag{29}$$

Using Eq. (12) and considering surface effects and following definitions for inertia of the microbeam:

$$\begin{Bmatrix} J_0 \\ J_1 \\ J_2 \\ J_3 \\ J_4 \\ J_5 \end{Bmatrix} = \int_{-h/2}^{h/2} \rho(z)\begin{Bmatrix} 1 \\ z \\ z^2 \\ f(z) \\ f^2(z) \\ zf(z) \end{Bmatrix} dz + \oint \rho^s(z)\begin{Bmatrix} 1 \\ z \\ z^2 \\ f(z) \\ f^2(z) \\ zf(z) \end{Bmatrix} dS \tag{30}$$

Eq. (29) can be written as follows:

$$T = \frac{b}{2}\int_0^L \left\{ J_0\left[\left(\frac{\partial u}{\partial t}\right)^2 + \left(\frac{\partial w}{\partial t}\right)^2\right] + J_2\left(\frac{\partial^2 w}{\partial x \partial t}\right)^2 + J_4\left[\left(\frac{\partial^2 w}{\partial x \partial t}\right)^2 + \left(\frac{\partial \Psi}{\partial t}\right)^2 - 2\frac{\partial^2 w}{\partial x \partial t}\frac{\partial \Psi}{\partial t}\right] - 2J_1\frac{\partial u}{\partial t}\frac{\partial^2 w}{\partial x \partial t} + 2J_3\left(\frac{\partial u}{\partial t}\frac{\partial^2 w}{\partial x \partial t} - \frac{\partial u}{\partial t}\frac{\partial \Psi}{\partial t}\right) - 2J_5\left[\left(\frac{\partial^2 w}{\partial x \partial t}\right)^2 - \frac{\partial^2 w}{\partial x \partial t}\frac{\partial \Psi}{\partial t}\right]\right\} dx \tag{31}$$

Variation in the kinetic energy of the microbeam can be expressed as follows:

$$\delta T = b\int_0^L \left(J_0 \frac{\partial u}{\partial t}\frac{\partial \delta u}{\partial t} + J_0 \frac{\partial w}{\partial t}\frac{\partial \delta w}{\partial t} + J_4 \frac{\partial \Psi}{\partial t}\frac{\partial \delta \Psi}{\partial t} - J_3 \frac{\partial u}{\partial t}\frac{\partial \delta \Psi}{\partial t} - J_3 \frac{\partial \Psi}{\partial t}\frac{\partial \delta u}{\partial t} + J_7 \frac{\partial^2 w}{\partial x\partial t}\frac{\partial^2 \delta w}{\partial x\partial t} - J_8 \frac{\partial^2 w}{\partial x\partial t}\frac{\partial \delta \Psi}{\partial t} - J_6 \frac{\partial^2 w}{\partial x\partial t}\frac{\partial \delta u}{\partial t} - J_6 \frac{\partial u}{\partial t}\frac{\partial^2 \delta w}{\partial x\partial t} - J_8 \frac{\partial \Psi}{\partial t}\frac{\partial^2 \delta w}{\partial x\partial t}\right) dx \tag{32}$$

where:

$$J_6 = J_1 - J_3$$
$$J_7 = J_2 + J_4 - 2J_5 \tag{33}$$
$$J_8 = J_4 - J_5$$

4.3. External work

The effects of the surrounding elastic medium on the sandwich microbeam, which is simulated with the viscoelastic Winkler-Pasternak model are considered as follows [37]:

$$q_f = -k_w w + k_g \frac{\partial^2 w}{\partial x^2} - C\frac{\partial w}{\partial t} \tag{34}$$

in which:
- k_w is the vertical stiffness coefficient (Winkler Spring coefficient).
- k_g is the shear stiffness coefficient of the foundation, which accounts for the transfer of shear forces between different points of the foundation.
- C is the viscoelastic damping coefficient of the foundation (damping coefficient), representing the energy dissipation in the foundation.

The extended force due to residual stress on the surface of the microbeam is calculated based on the Laplace-Young equation, as fallows [4]:

$$q_s = H_s \frac{\partial^2 w}{\partial x^2} \tag{35}$$

where, H_s for a rectangular cross-section can be expressed:

$$H_s = \tau_s\big|_{z=-h/2} + \tau_s\big|_{z=h/2} \tag{36}$$

Finally, the external work done by non-conservative loads, and after that, the virtual work can be stated as:

$$W_{n.c.} = b\int_0^L (q_s + q_f) w dx$$
$$\delta W_{n.c.} = b\int_0^L (q_s + q_f)\delta w dx \tag{37}$$

4.4. The governing equations of motion

Substituting Eqs. (26), (32) and (37) into Eq. (18) and integrating by parts, the set of governing equations can be presented as:

$$\delta u: -J_0\frac{\partial^2 u}{\partial t^2} + (J_6 - b_1)\frac{\partial^3 w}{\partial t^2\partial x} + J_3\frac{\partial^2 \Psi}{\partial t^2} + B_0\frac{\partial^2 u}{\partial x^2} + C_1\frac{\partial^3 w}{\partial x^3} - B_3\frac{\partial^2 \Psi}{\partial x^2} = 0$$

$$\delta w: J_6\frac{\partial^3 u}{\partial t^2\partial x} - (J_7 + b_5 - b_2)\frac{\partial^4 w}{\partial t^2\partial x^2} + J_0\frac{\partial^2 w}{\partial t^2} + J_8\frac{\partial^3 \Psi}{\partial t^2\partial x} + c\frac{\partial w}{\partial x} + (B_3 - B_1)\frac{\partial^3 u}{\partial x^3} + \left(C_3 - C_2 + 2l^2 m_0 - 2l^2 m_1 + \frac{l^2}{2}m_2\right)\frac{\partial^4 w}{\partial x^4} - \left(B_6 + \frac{l^2}{2}m_3 + H_s + k_g\right)\frac{\partial^2 w}{\partial x^2} + k_w w + \left(B_4 + B_5 + l^2 m_1 - \frac{l^2}{2}m_2\right)\frac{\partial^3 \Psi}{\partial x^3} + \left(A_6 + \frac{l^2}{2}m_3\right)\frac{\partial \Psi}{\partial x} = 0 \tag{38}$$

$$\delta \Psi: J_3\frac{\partial^2 u}{\partial t^2} + (J_8 + b_5)\frac{\partial^3 w}{\partial t^2\partial x} - J_4\frac{\partial^2 \Psi}{\partial t^2} - B_3\frac{\partial^2 u}{\partial x^2} + \left(-C_3 + l^2 m_1 - \frac{l^2}{2}m_2\right)\frac{\partial^3 w}{\partial x^3} + \left(B_6 + \frac{l^2}{2}m_3\right)\frac{\partial w}{\partial x} + \left(B_4 + \frac{l^2}{2}m_2\right)\frac{\partial^2 \Psi}{\partial x^2} - \left(A_6 + \frac{l^2}{2}m_3\right)\Psi = 0$$

In this paper, two types of boundary conditions are considered for each edge of the microbeam. The fixed state (Clamped support (C)) and the simple state (Simply support (S)) are considered as fallow:

Clamped support: $u=0, \quad w=0, \quad \frac{\partial w}{\partial x}=0, \quad \Psi=0,$

Simply support: $\frac{\partial u}{\partial x}=0, \quad w=0, \quad \frac{\partial^2 w}{\partial x^2}=0 \quad \frac{\partial \Psi}{\partial x}=0$

Also, by solving the Eq. (18).

$$B_1\frac{\partial u}{\partial x}+[C_2+l^2(m_1-2m_0)]\frac{\partial^2 w}{\partial x^2}-(B_5+l^2m_1)\frac{\partial \Psi}{\partial x}=0$$
$$B_3\frac{\partial u}{\partial x}+\left[C_3+l^2\left(\frac{m_2}{2}-m_1\right)\right]\frac{\partial^2 w}{\partial x^2}-\left(B_4+\frac{l^2m_2}{2}\right)\frac{\partial \Psi}{\partial x}=0 \tag{39}$$

Finally, by using Eqs. (39) and (27), the motion equations (Eq. (38)) can be written in the following dimensionless form:

$$\delta u: \lambda^2\left[-J_0^*U+(J_6^*-b_1^*)\frac{dW}{d\zeta}+J_3^*\Psi\right]+B_0^*\frac{d^2U}{d\zeta^2}+C_1^*\frac{d^3W}{d\zeta^3}-B_3^*\frac{d^2\Psi}{d\zeta^2}=0$$
$$\delta w: \lambda^2\left[J_6^*\frac{dU}{d\zeta}-(J_7^*+b_5^*-b_2^*)\frac{d^2W}{d\zeta^2}+J_0^*W+J_8^*\frac{d\Psi}{d\zeta}\right]+\lambda c^*W+(B_3^*+B_1^*)\frac{d^3U}{d\zeta^3}+[C_3^*-C_2^*+\gamma^2(2m_0^*-2m_1^*+m_2^*)]\frac{d^4W}{d\zeta^4}-\left(B_6^*+\gamma^2m_3^*+H_s^*+k_g^*\right)\frac{d^2W}{d\zeta^2}+k_w^*W+[-B_4^*+B_5^*]+\gamma^2(m_1^*-m_2^*)\frac{d^3\Psi}{d\zeta^3}+(A_6^*+\gamma^2m_3^*)\frac{d\Psi}{d\zeta}=0 \tag{40}$$
$$\delta\Psi: \lambda^2\left[J_3^*U+(J_8^*+b_5^*)\frac{dW}{d\zeta}-J_4^*\Psi\right]-B_3^*\frac{d^2U}{d\zeta^2}+[-C_3^*+\gamma^2(m_1^*-m_2^*)]\frac{d^3W}{d\zeta^3}+(B_6^*+\gamma^2m_3^*)\frac{dW}{d\zeta}+(B_4^*+\gamma^2m_2^*)\frac{d^2\Psi}{d\zeta^2}-(A_6^*+\gamma^2m_3^*)\Psi=0$$

in which, the dimensionless parameters are defined as follows:

$$\zeta=\frac{x}{L}, \qquad \tau=\frac{t}{L}\sqrt{\frac{E_m}{\rho_m}}$$
$$\begin{Bmatrix}u(\zeta,\tau)\\w(\zeta,\tau)\\\Psi(\zeta,\tau)\end{Bmatrix}=\begin{Bmatrix}LU(\zeta)\\LW(\zeta)\\\Psi(\zeta)\end{Bmatrix}e^{\lambda\tau}$$
$$\begin{Bmatrix}B_0^*\\B_6^*\end{Bmatrix}=\frac{1}{E_mL}\begin{Bmatrix}B_0\\B_6\end{Bmatrix}, \quad \begin{Bmatrix}B_1^*\\B_3^*\end{Bmatrix}=\frac{1}{E_mL^2}\begin{Bmatrix}B_1\\B_3\end{Bmatrix}, \quad \begin{Bmatrix}B_4^*\\B_5^*\end{Bmatrix}=\frac{1}{E_mL^3}\begin{Bmatrix}B_4\\B_5\end{Bmatrix}, \quad \begin{Bmatrix}C_2^*\\B_3^*\end{Bmatrix}=\frac{1}{E_mL^3}\begin{Bmatrix}C_2\\C_3\end{Bmatrix}$$
$$\begin{Bmatrix}m_0^*\\m_1^*\\m_2^*\end{Bmatrix}=\frac{1}{E_mL}\begin{Bmatrix}m_0\\m_1\\0.5m_2\end{Bmatrix}$$
$$\begin{Bmatrix}b_2^*\\b_5^*\end{Bmatrix}=\frac{1}{\rho_mL^3}\begin{Bmatrix}b_2\\b_5\end{Bmatrix}, \quad \begin{Bmatrix}J_3^*\\J_6^*\end{Bmatrix}=\frac{1}{\rho_mL^2}\begin{Bmatrix}J_3\\J_6\end{Bmatrix}, \quad \begin{Bmatrix}J_4^*\\J_5^*\\J_7^*\\J_8^*\end{Bmatrix}=\frac{1}{\rho_mL^3}\begin{Bmatrix}J_4\\J_5\\J_7\\J_8\end{Bmatrix} \tag{41}$$
$$c^*=\frac{c}{\sqrt{\rho_mE_m}}, \quad C_1^*=\frac{C_1}{E_mL^2}$$
$$b_1^*=\frac{b_1}{\rho_mL^2}, \quad A_6^*=\frac{A_6}{E_mL}$$
$$m_2^*=\frac{m_3L}{2E_m}, \quad J_0^*=\frac{J_0}{\rho_mL}$$
$$k_w^*=\frac{k_wL}{E_m}, \quad k_g^*=\frac{k_g}{E_mL}$$
$$H_s^*=\frac{H_s}{E_mL}, \quad \gamma=\frac{l}{L}$$

5. The solution technique

Dimensionless motion equations can be written by defining time variable $\tau = \frac{t}{L}\sqrt{\frac{E_m}{\rho_m}}$ and space variable $\zeta = \frac{x}{L}$, in a dimensionless form using separation of variables in the form of Eq. (42):

$$\begin{Bmatrix} u(\zeta,\tau) \\ w(\zeta,\tau) \\ \Psi(\zeta,\tau) \end{Bmatrix} = \begin{Bmatrix} LU(\zeta) \\ LW(\zeta) \\ \Psi(\zeta) \end{Bmatrix} e^{\lambda\tau} \tag{42}$$

in which λ is a dimensionless eigenvalue.

In the present study, the DQM approach is used for obtaining relatively accurate numerical results for a considerably smaller number of grid points. DQM is a higher-order numerical method that provides a highly rapid solution for linear and nonlinear partial differential equations. This method replaces the spatial derivatives $(0 \le x \le l)$ of a function F by an algebraic summation. So, the values of the function at these dots will be a column vector as shown below [38]:

$$\{f\} = \begin{Bmatrix} f_1 \\ f_2 \\ \vdots \\ f_{N-1} \\ f_N \end{Bmatrix} = \begin{Bmatrix} f_{(x_1)} \\ f_{(x_2)} \\ \vdots \\ f_{(x_{N-1})} \\ f(x_{N-1}) \end{Bmatrix} \tag{43}$$

Based on the DQM, the kth order derivative of this function is estimated in the mentioned points as follows [39]:

$$\begin{Bmatrix} \frac{d^k f}{dx^k} \end{Bmatrix} = \left[A^{(k)}\right]_{N\times N}\{\mathrm{f}\} \tag{44}$$

where $A^{(k)}$ is the weighting coefficients associated with kth order partial derivative of F, and N is the number of grid points in longitudinal direction:

$$A_{ij}^{(1)} = \begin{cases} \dfrac{\prod\limits_{\substack{m=1 \\ m\neq i,j}}^{N}\left(x_i - x_m\right)}{\prod\limits_{\substack{m=1 \\ m\neq j}}^{N}\left(x_j - x_m\right)} & i \neq j \\ \sum\limits_{\substack{m=1 \\ m\neq i}}^{N} \dfrac{1}{x_i - x_m} & i = j \end{cases} \quad i,j = 1,2,\ldots,N, \tag{45}$$

While that for higher derivatives using:

$$\left[A^{(k)}\right] = \left[A^{(1)}\right]\left[A^{(k-1)}\right] \qquad k = 2,3,\ldots,N-1 \tag{46}$$

In DQM, one of the most important points in accelerating convergence is the distribution of the points. The non-uniform Chebyshev–Gauss–Lobatto nodal distribution has a well-accepted set of the grid points and is expressed as [39]:

$$x_m = \frac{L}{2}\left\{1 - \cos\left[\pi\frac{m-1}{N-1}\right]\right\} \qquad m = 1,2,3,\ldots,N \tag{47}$$

Applying DQM to final equations and using Eq. (44) the governing motion equations and the boundary conditions can be expressed as a system of algebraic equations as follows:

$$[\mathrm{M}]\{\ddot{\mathrm{S}}\} + [\mathrm{C}]\{\dot{\mathrm{S}}\} + [\mathrm{K}]\{\mathrm{S}\} = \{0\}$$

Or (48)

$$\lambda^2[\mathrm{M}]\{\mathrm{S}\} + \lambda[\mathrm{C}]\{\mathrm{S}\}[\mathrm{K}]\{\mathrm{S}\} = \{0\}$$

where $[M]$, $[C]$, and $[K]$ are, mass, damping, and stiffness matrices, respectively and $\{s\}$ is a column vector known as the displacement vector. Considering boundary conditions into the final equations, the eigenvalues of the state-space matrix as dimensionless frequency are obtained [40].

$$\left([state - space] = \begin{bmatrix} [0] & [\mathrm{I}_x] \\ -[\mathrm{M}^{-1}\mathrm{K}] & -[\mathrm{M}^{-1}\mathrm{C}] \end{bmatrix}\right) \tag{49}$$

In which $[I]$ and $[0]$ are the unitary and zero matrices; by solving the eigenvalue problem presented in Eq. (49), the eigenvalues are obtained in a complex form. The dimensionless frequencies and the corresponding damping coefficient are obtained using the real part and imaginary part of the extracted eigenvalues [41].

6. Numerical results and discussion

6.1. Overview

In this section, in addition to the verification and convergent example, parametric studies are accomplished. In the parametric study, the influences of the porous core thickness, porosity coefficient, pore distribution pattern, CNTs mass fraction, type and distribution patterns, the intensity and higher percentage of carbon nanotube clustering, material length scale parameter, different boundary conditions, and parameters of the viscoelastic WinklerPasternak foundation on the natural frequencies and damping coefficients of the microbeam are investigated. The presented results correspond to a microbeam with clamped and simply supported conditions (CS). This microbeam has a material length scale parameter $\gamma = 0.01$ and geometric properties $L = 20\mu m$, $\frac{b}{L} = 0.02$, $\frac{h}{L} = 0.01$ and $\frac{h_c}{h} = 0.8$ and the following magnitudes of the coefficients of the viscoelastic foundation are $k_w^* = k_g^* = c^* = 0.0001$. Furthermore, the porous core of the microbeam is made of epoxy polymer with properties $E_m = 2.1GPa$, $\upsilon_m = 0.34$ and $\rho_m = 1150\frac{kg}{m^3}$ [missing property please specify if needed]. Additionally, the nanocomposite facesheets of the microbeam consist of polymer reinforced with single-walled carbon nanotubes CNT (10,10) at a volume fraction of $w_r = 0.01$. These CNTs are distributed following the AV pattern in both the lower and upper facesheets.

The agglomeration coefficients of the carbon nanotubes in the facesheets are defined as $\eta = 0.8$ and $\mu = 0.8$. Finally, the surface effect properties of the carbon nanotube-reinforced polymer microbeam are defined by $E^s = 1.22\frac{N}{m}$, $\tau^s = 0.89\frac{N}{m}$ and $\rho^s = 10^{-7}\frac{kg}{m^2}$. It is important to note that all results are presented in nondimensional form, and except where explicitly stated, all nondimensional parameters are defined according to Eq. (41).

6.2. Convergence studies

To choose the proper number of grid points, a sandwich micro beam fabricated from the materials defined in section 6.1. is considered. Figure 5 has been plotted to investigate the convergence of grid points and as can be seen from the figure, the natural frequency converts to the constant value after $N = 13$. Also, in Table 1, the natural frequencies of the microbeam are presented based on Reddy's theory and computed using the DQM for various numbers of grid points. As may be noted, the numerical solution exhibits excellent convergence behavior; specifically, reliable results for the natural frequencies (Ω) and damping coefficients (ζ) across different vibration modes can be achieved using only $N = 13$ grid points. Therefore, the $N = 13$ mesh size is chosen for the extraction of the next results.

Table 1. Convergence analysis for the sandwich micro beam

	Mode	First	Second	Third	Fourth
Ω	N=5	0.4571	3.1151	6.8857	8.7874
	N=7	0.4423	0.8875	1.3366	3.1223
	N=9	0.4369	0.8889	1.4268	1.9221
	N=11	0.4352	0.8829	1.4085	2.0453
	N=13	0.4344	0.8817	1.4052	2.0027
	N=15	0.4339	0.8815	1.4031	2.0055
	N=17	0.4336	0.8814	1.4018	2.0049
	N=19	0.4334	0.8814	1.4010	2.0048
ζ	N=5	0.0055	0.0000	0.0000	0.0000
	N=7	0.0055	0.0055	0.0055	0.0000
	N=9	0.0055	0.0055	0.0055	0.0054
	N=11	0.0055	0.0055	0.0055	0.0054
	N=13	0.0055	0.0055	0.0055	0.0054
	N=15	0.0055	0.0055	0.0055	0.0054
	N=17	0.0055	0.0055	0.0055	0.0054
	N=19	0.0055	0.0055	0.0055	0.0054

6.3. Verification of the results

To verify the accuracy of the formulation and the solution procedure, the results of the present work are compared with the available results in the literature. Consider a single-layer porous microbeam with a length of $L = 1m$ and a Poisson's ratio of $\upsilon = 1.3$.

The pore distribution is symmetric of the first type (SI), and the porosity coefficient is $e_1 = 0.5$.

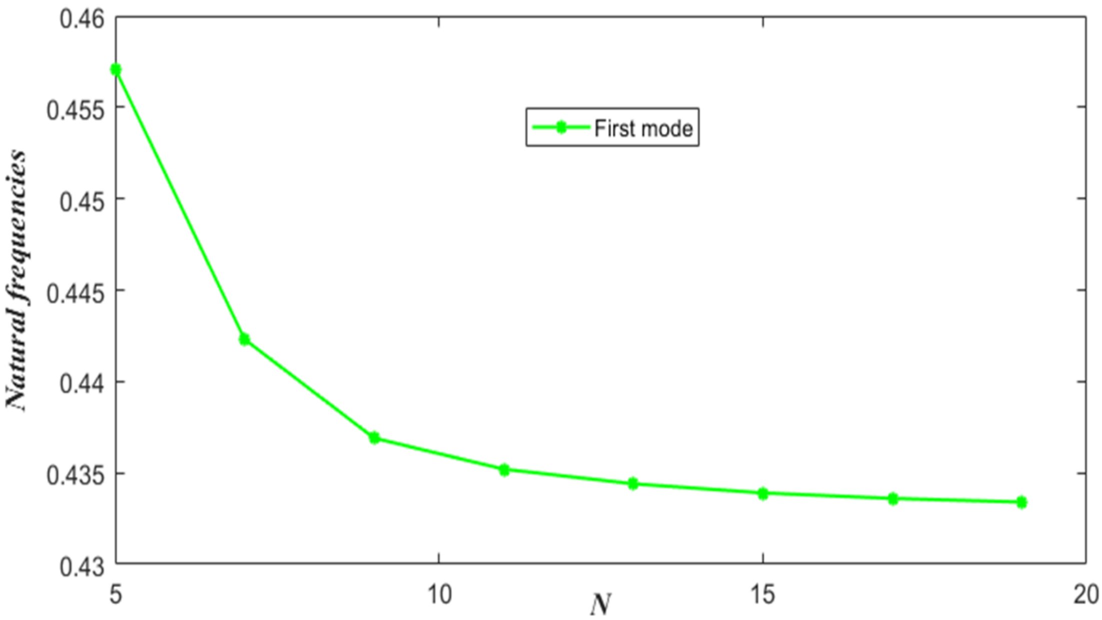

Figure 5. Convergence of grid points

By neglecting surface fluid effect, the dimensionless natural frequencies of the beam, defined as $\Omega^* = wL\sqrt{\rho(1-\upsilon^2)/E}$, are presented in Table 2 for various boundary conditions and different values of the thickness-to-length ratio.
These results are compared alongside those reported by Chen et al. [6] based on the Ritz method and ANSYS software are also presented in this table.
As observed, the results show a good agreement and confirm the validity of the presented analysis.
The minor discrepancies can be attributed to differences in beam modeling theories and the solution method. In reference [6], the beam is modelled by ANSYS software and is compared with the Ritz method based on the first-order shear deformation theory, which is less accurate compared to the third-order shear deformation theory employed in this study.

Table 2. A comparison between the present prediction for dimensionless natural frequencies of a porous single-layered beam in its first vibrational mode and those of ref. [6]

			SS	CS	CC
L/h =10	Present	DQM	0.2882	0.4374	0.6146
	Chen et al. [6]	Ritz	0.2798	0.4242	0.5944
	Chen et al. [6]	ANSYS	0.2778	0.4227	0.6101
	Difference (%)		3.00	3.11	0.73
L/h =20	Present	DQM	0.0589	0.0920	0.1332
	Chen et al.	Ritz	0.0571	0.0891	0.1291
	Chen et al. [6]	ANSYS	0.0571	0.0891	0.1289
	Difference (%)		3.15	3.25	3.18

6.4. Parametric studies

In this section, the different parametric studies are investigated.
Figure 6 illustrates the influence of the porous core thickness on the natural frequencies and damping coefficients.
As can be seen, the simultaneous reduction of stiffness and mass leads to a nonlinear behavior of the natural frequencies of the microbeam as the core-to-total thickness ratio increases.
The simultaneous reduction of stiffness and mass leads to a nonlinear behavior of the natural frequencies of the microbeam as the core-to-total thickness ratio increases. The fundamental mode frequency exhibits an optimal peak, while the frequencies of the third and fourth modes decrease. Furthermore, increasing the thickness of the viscoelastic porous core enhances energy dissipation, resulting in a uniform increase in damping coefficients. Surface forces remain constant, maintaining a linear trend in damping behavior.
Figure 7 displays the effect of the porosity coefficient on the natural frequencies and damping ratios of the microbeam.
By increasing the porosity coefficient, stiffness decreases slightly, and the microbeam's mass decreases significantly, leading to an increase in the natural frequencies.
Additionally, higher porosity increases the volume of core cavities, enhancing vibrational energy absorption and uniformly increasing damping coefficients. Table 3 compares the influence of the three different pore distribution patterns on the natural frequencies and damping coefficients of the microbeam.
It may be noted that the highest natural frequencies correspond to the *SI* distribution pattern, where larger pores are located near the mid-surface and result in the least reduction in bending stiffness.

Table 3. Effect of the pore distribution pattern on the natural frequencies and damping coefficients

		First mode	Second mode	Third mode	Fourth mode
λ	U	0.4345	0.8820	1.4057	2.0036
	SI	0.4347	0.8829	1.4085	2.0093
	SII	0.4344	0.8817	1.4052	2.0027
ζ	U	0.0055	0.0055	0.0055	0.0055
	SI	0.0055	0.0055	0.0055	0.0054
	SII	0.0055	0.0055	0.0055	0.0054

Increasing the mass fraction of CNTs strengthens the microbeam structure and, while increasing stiffness, slightly reduces its mass.
These changes lead to an increase in natural frequencies and a decrease in damping coefficients, as clearly showed in Figure 8.
Table 4 demonstrates the influences of the type of CNT on the natural frequencies of the microbeam.
It can be investigated that CNTs with smaller chiral indices and consequently smaller diameters and higher elastic constants lead to an increase in the natural frequencies.
Furthermore, the type of the nanotube has no significant effect on the damping behaviour, and the damping ratios remain almost constant for all vibration modes and for all types of nanotubes.

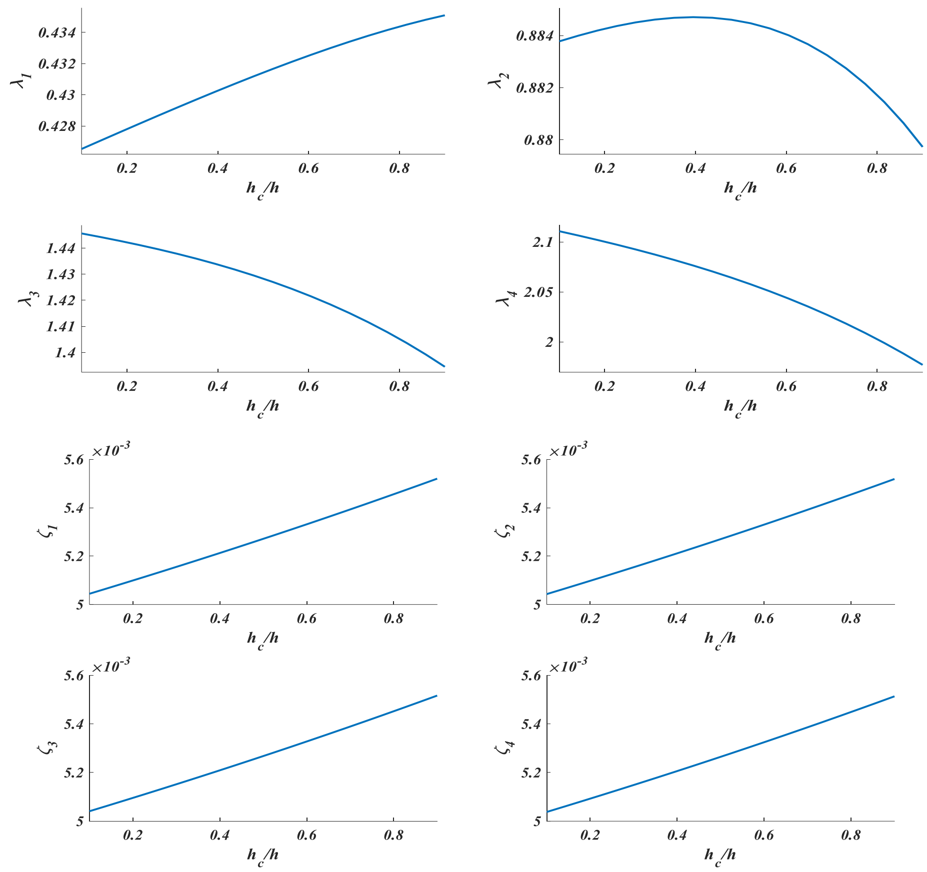

Figure 6. Effect of the porous core thickness on the natural frequencies and damping coefficients of the sandwich microbeam

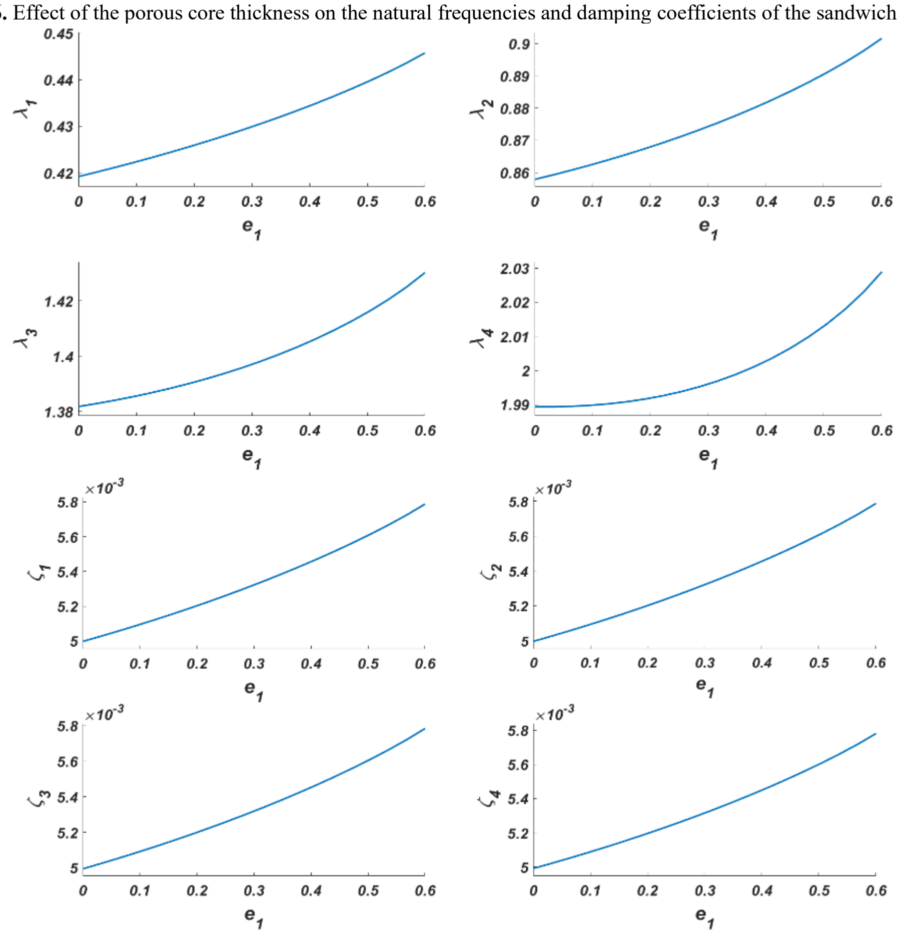

Figure 7. Effect of the porosity coefficient on the natural frequencies and damping ratios of the sandwich microbeam

10.57647/jsm.2026.1801.03

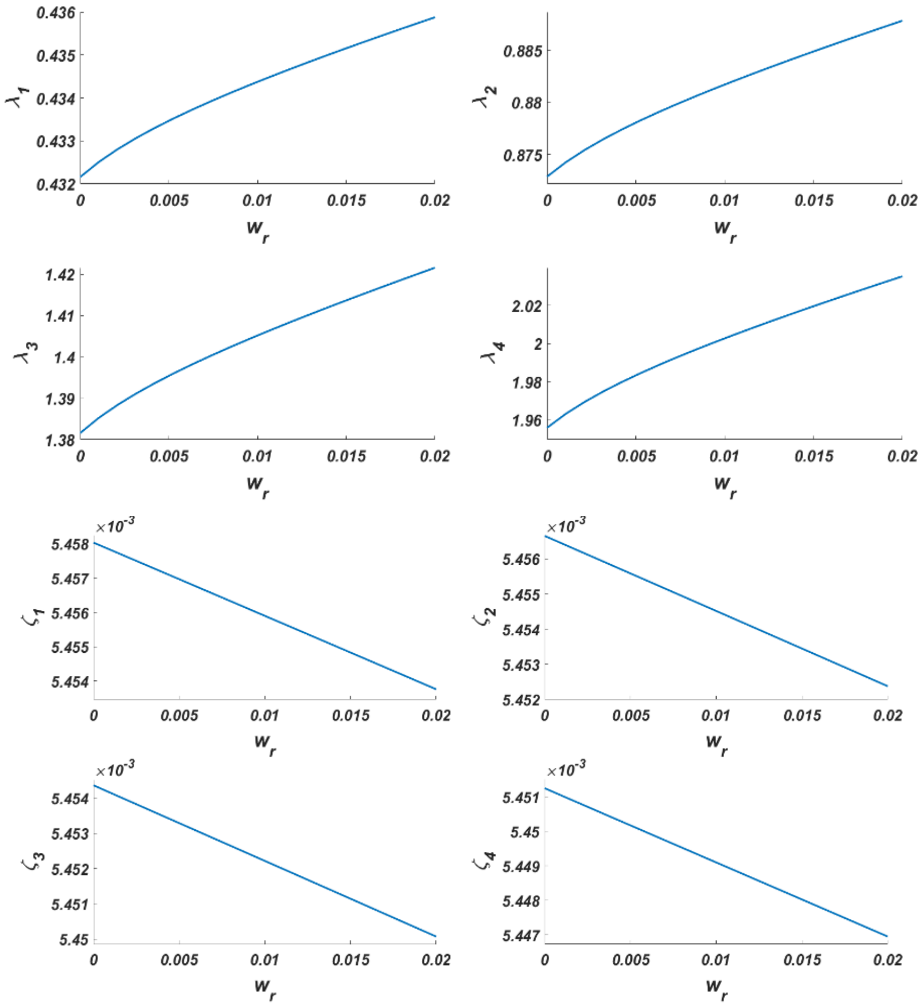

Figure 8. Effect of the CNT mass fraction on the natural frequencies and damping coefficient

Table 4. Effect of the CNT type on the natural frequencies and damping ratios

	Mode	(5,5)	(10,10)	(15,15)	(20,20)	(50,50)
λ	First	0.4359	0.4344	0.4338	0.4334	0.4327
	Second	0.8876	0.8817	0.8794	0.8780	0.8751
	Third	1.4207	1.4052	1.3990	1.3955	1.3878
	Fourth	2.0333	2.0027	1.9905	1.9836	1.9684
ζ	First	0.0055	0.0055	0.0055	0.0055	0.0055
	Second	0.0055	0.0055	0.0055	0.0055	0.0055
	Third	0.0055	0.0055	0.0055	0.0055	0.0055
	Fourth	0.0054	0.0054	0.0054	0.0054	0.0054

Table 5 depicts the impact of the CNT distribution pattern on the natural frequencies and damping coefficients of the sandwich microbeam. It is evident that the combination with the highest values of natural frequencies is AV and UU. In contrast, the lowest values belong to the VA combination. So, it can be inferred that to maximize the natural frequencies of the microbeam, CNTs should be distributed as close as possible to the microbeam's top and bottom surfaces.

Table 5. Influence of the carbon nanotube distribution pattern on the natural frequencies and damping ratios of the sandwich microbeam

		First	Second	third	fourth
λ	UU	0.4344	0.8819	1.4058	2.0039
	AA	0.4343	0.8815	1.4047	2.0018
	VV	0.4343	0.8815	1.4047	2.0018
	XX	0.4343	0.8815	1.4047	2.0018
	OO	0.4343	0.8815	1.4047	2.0017
	VA	0.4343	0.8814	1.4042	2.0008
	AV	0.4344	0.8817	1.4052	2.0027
ζ	UU	0.0055	0.0055	0.0055	0.0054
	AA	0.0055	0.0055	0.0055	0.0054
	VV	0.0055	0.0055	0.0055	0.0054
	XX	0.0055	0.0055	0.0055	0.0054
	OO	0.0055	0.0055	0.0055	0.0054
	VA	0.0055	0.0055	0.0055	0.0054
	AV	0.0055	0.0055	0.0055	0.0054

Explanation for this statement is that this distribution pattern causes the maximum rise in the bending stiffness of the microbeam. All in all, the impact of the CNT distribution pattern is not a very important effect on the natural frequences. Also, the CNT distribution pattern has no significant effect on the damping ratios. Effects of the agglomeration coefficient η on the natural frequencies and damping ratios are inspected in Figure 9, and an increase in the agglomeration coefficient η means a higher percentage of CNTs has accumulated. This figure shows that with increasing the agglomeration coefficient η, the natural frequencies decrease in all vibration modes, because the agglomeration leads to a decrease in the elastic constants of the nanocompsite. In Table 5, among CNT distribution patterns, the XX pattern yields the highest natural frequencies (e.g., 0.4345 for first mode, ~0.02-0.1% higher than others) due to its cross-ply configuration enhancing bidirectional stiffness and elastic moduli, as per standard CNT composite mechanics. This superior performance of XX over UU, VV, etc., aligns with physical expectations for reinforced microbeams. Furthermore, the vibration energy absorption significantly increases, enhancing the damping capacity of the microbeam.

Figure 10 reflects that increasing the agglomeration coefficient μ, which is related to the decrease in the intensity of CNT clustering, leads to an increase in the natural frequencies and stiffness of the microbeam, while the damping capacity decreases significantly due to the decrease in vibration energy absorption.

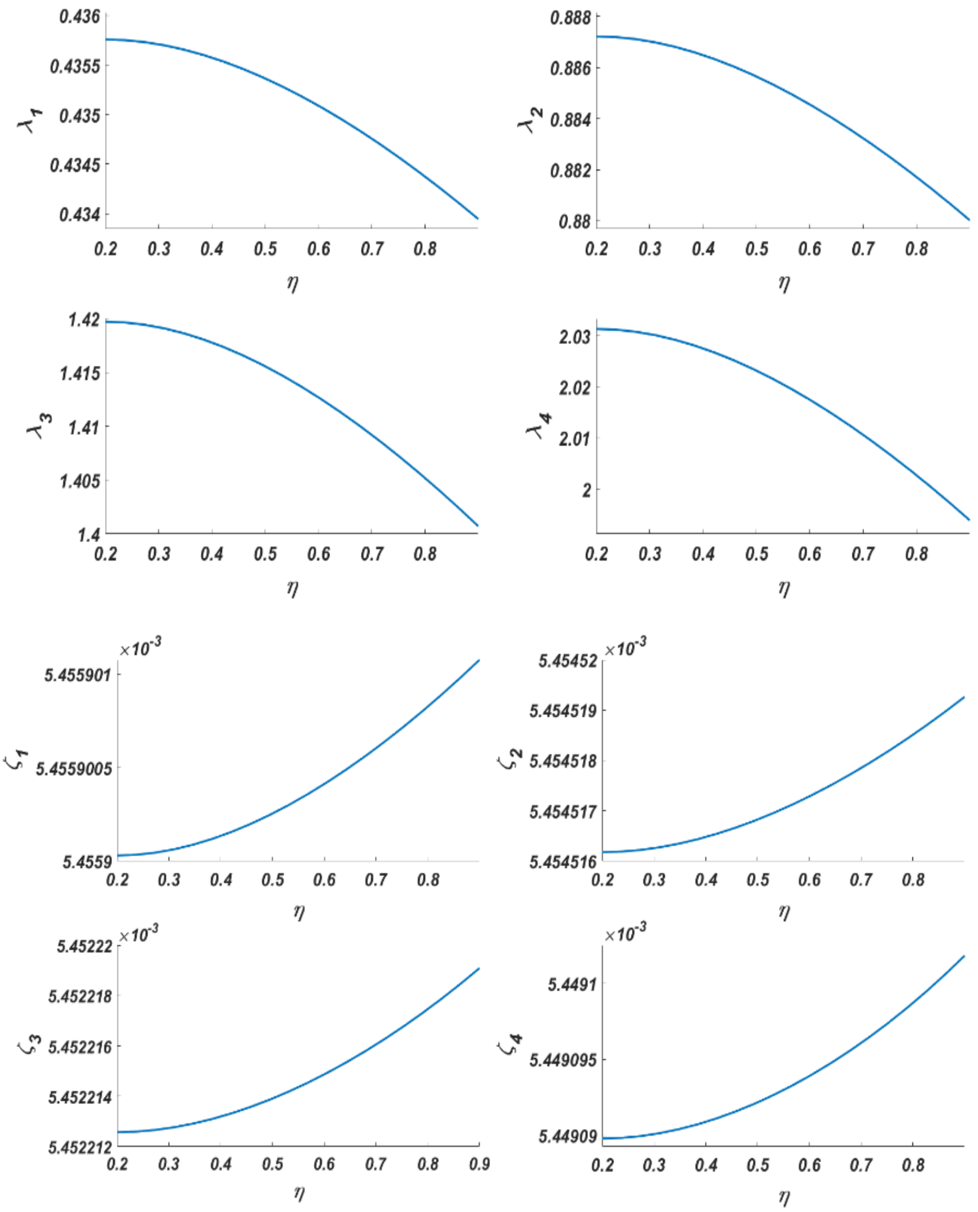

Figure 9. Effect of the agglomeration coefficient η on the natural frequencies and damping ratios of the sandwich microbeam

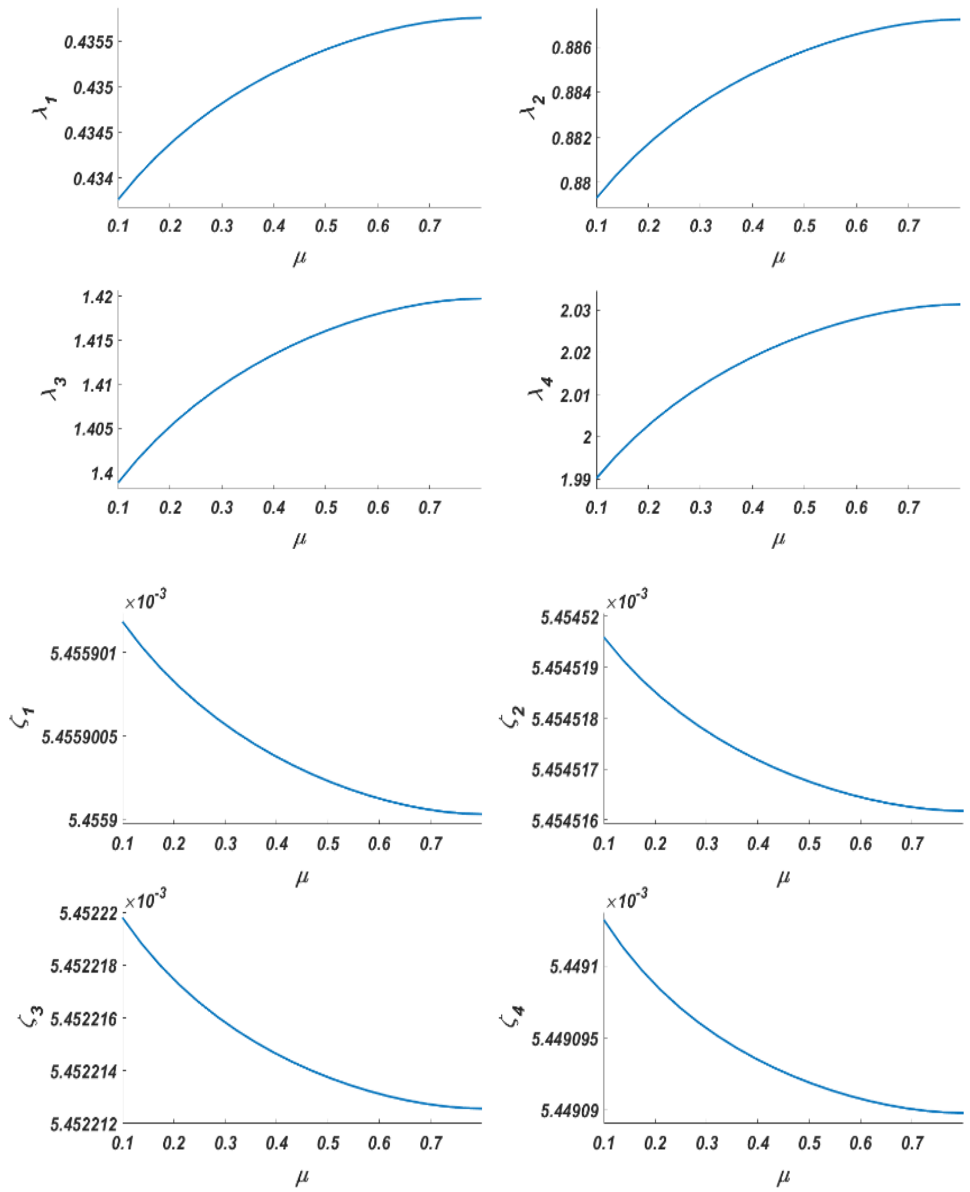

Figure 10. Effect of the agglomeration coefficient μ on the natural frequencies and damping ratios

The influence of the material length scale parameter on the natural frequencies and damping ratios of the sandwich microbeam is displayed in Figure 11. This figure confirms that increasing the material length scale parameter leads to greater stiffness and consequently higher natural frequencies of the microbeam. Figure 10 reveals that as the dimensionless material length scale parameter rises from 0.00 to 0.02, the dimensionless first natural frequency increases by nearly 11 percent. Moreover, the damping ratios in the first to third modes exhibit a nonlinear trend initially increasing and then decreasing due to the dominance of the stiffening effect at lower values and the reduced contribution of shear modes and energy redistribution at higher values. In the fourth mode, the damping ratio initially increases slightly, remains nearly constant, and then rises significantly at higher scale parameter values due to the mode's higher sensitivity and reduced deformation. Figure 12 demonstrates the effects of the thickness-to-length ratio on the natural frequencies and damping ratios. It may be concluded from this figure that increasing the microbeam thickness leads to a simultaneous increase in both stiffness and mass; also, due to the higher power dependence of the mass in the governing equations, the mass increase dominates.

Consequently, the natural frequencies decrease in the first to third modes, while in the fourth mode, they initially decrease and then increase.

Furthermore, the damping ratios decrease nonlinearly with increasing thickness-to-length ratio, which is attributed to the decrease in vibration energy absorption capacity.

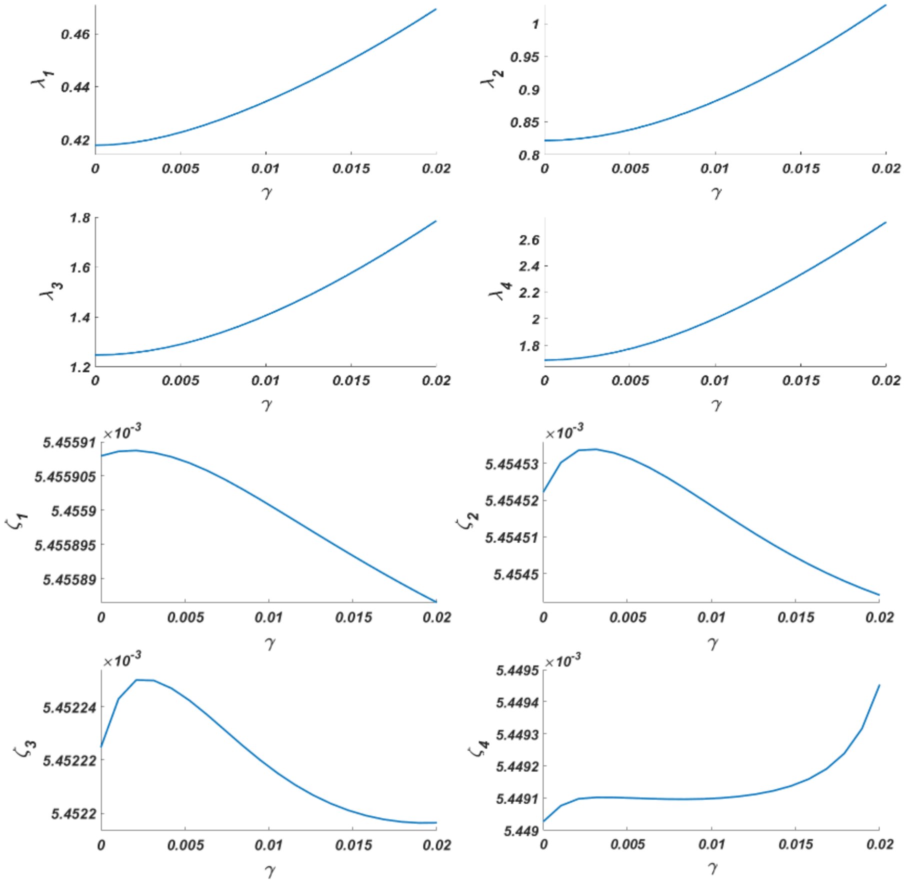

Figure 11. Effect of the material length scale parameter on the natural frequencies and damping ratios

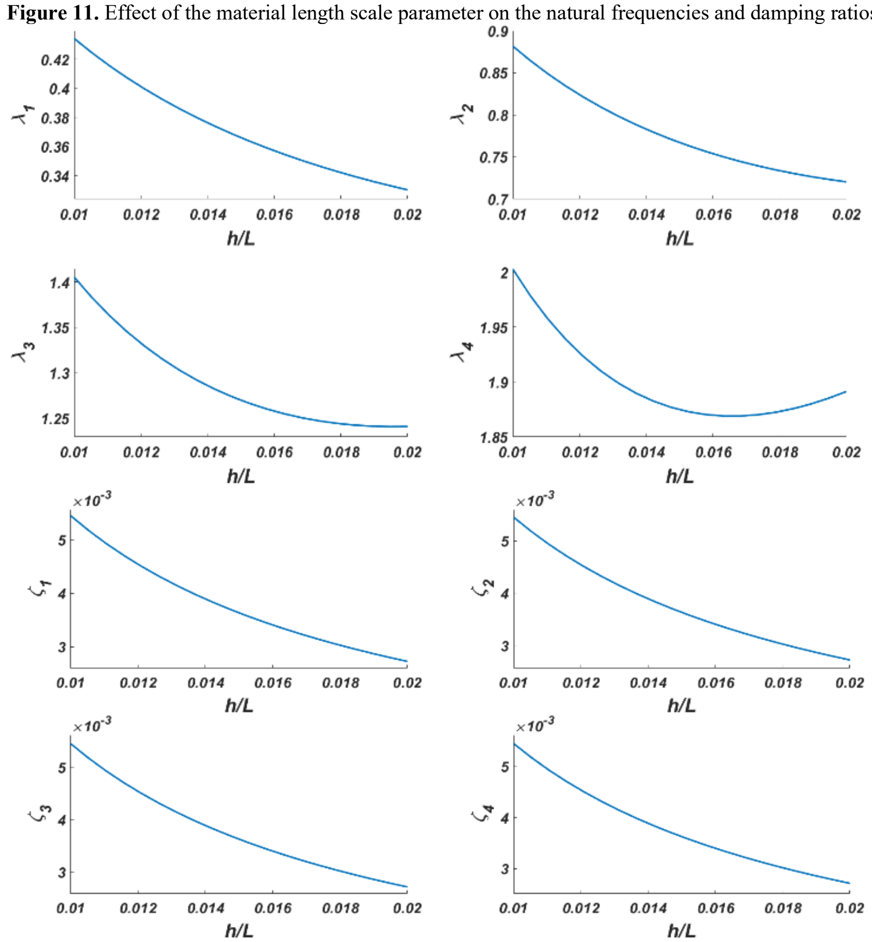

Figure 12. Effect of the thickness-to-length ratio on the natural frequencies and damping ratios

10.57647/jsm.2026.1801.03

Table 6 compares the dimensionless natural frequencies and damping ratios of three types of edge conditions for a sandwich microbeam that is supported by an elastic Winkler–Pasternak foundation.

This table proves that the microbeam with clamped clamped (CC) boundary conditions exhibit the highest natural frequencies due to greater boundary stiffness, while the simply supported (SS) microbeam has the lowest natural frequencies. Also, Figure 13 can better visualize these trends and shows the influences of the boundary conditions on the natural frequencies for first four frequencies.

Moreover, the damping ratios remain nearly constant across all vibration modes and boundary conditions, indicating that the boundary conditions have a negligible effect on the damping. Figure 14 reveals the impact of the elastic coefficient of the substrate on the natural frequencies and damping of the sandwich microbeam. Based on Eq. (34), an increase in K_w confirms a commensurate increasing in the potential energy of the substrate, hence a rise of high potential energy that enables high natural frequencies of all the vibrational modes. This figure demonstrates that when the K_w rises, there is a commensurate rise in potential energy, which generates high natural frequencies. Additionally, the damping ratios increase nonlinearly and significantly, indicating a substantial improvement in the vibration energy absorption capacity.

The influences of the foundation shear and damping coefficients on the natural frequencies and damping of the sandwich microbeam are presented in Figure 15 and 16. As can be seen from Figure 15, increasing the shear modulus of the foundation leads to an increase in the potential energy and natural frequencies across all vibration modes of the microbeam. Also, the damping ratios generally increase, with a slower growth rate in lower modes and a faster rate in higher modes, particularly in the fourth mode. The effect of the shear modulus on the natural frequency is more significant than that of the normal elastic modulus. Moreover, Figure 15 shows that an increase in the foundation damping coefficient leads to a nonlinear and accelerated decrease in the natural frequencies across all vibration modes, indicating a strong inhibitory effect of the foundation damping on the system vibrations. Additionally, the damping ratios of the microbeam increase uniformly and continuously, reflecting an improved vibration energy absorption capacity of the system.

Table 6. Effect of the boundary conditions on the natural frequencies and damping ratios

	λ			ζ		
	CC	CS	SS	CC	CS	SS
First mode	0.4595	0.4344	0.4107	0.0055	0.0055	0.0055
Second mode	0.9375	0.8817	0.8342	0.0055	0.0055	0.0055
Third mode	1.4887	1.4052	1.3242	0.0055	0.0055	0.0055
Fourth mode	2.1287	2.0027	1.8958	0.0054	0.0054	0.0054

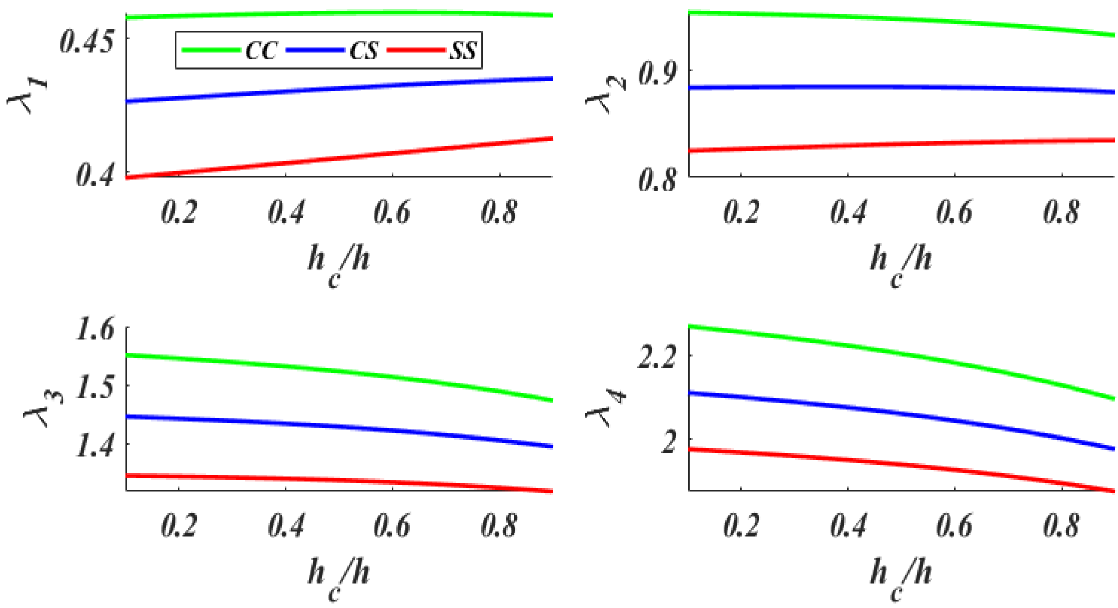

Figure 13. Influence of the boundary conditions on the natural frequences for first four frequencies

10.57647/jsm.2026.1801.03

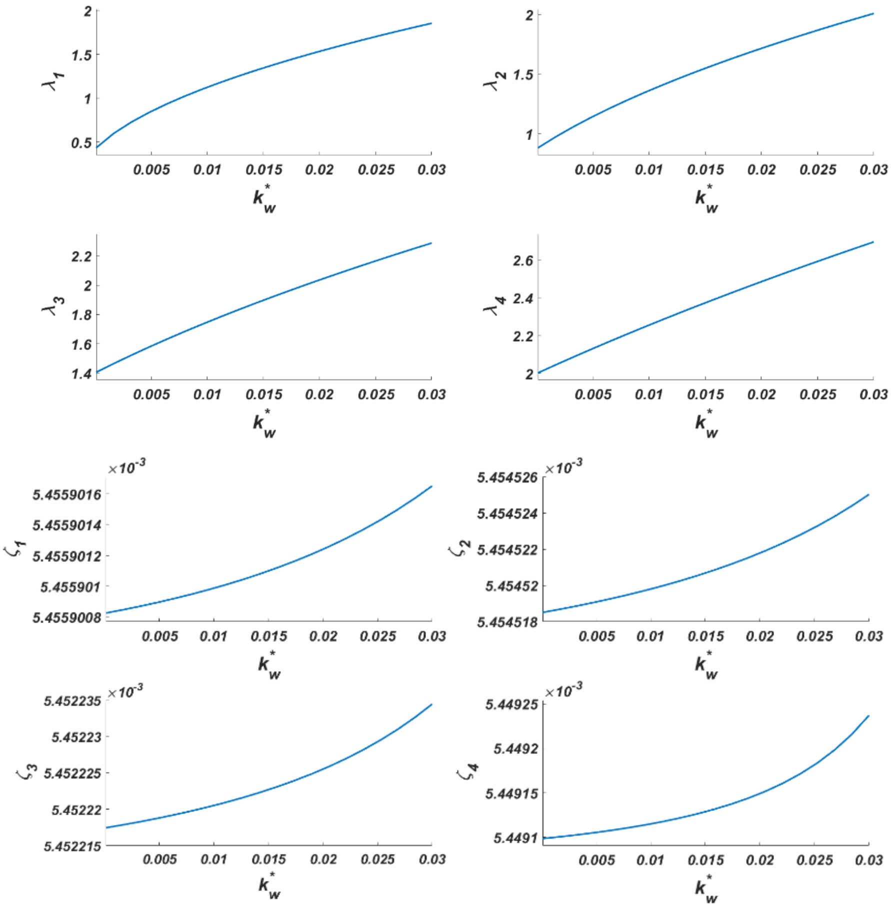

Figure 14. Influence of the elastic coefficient of the substrate on the natural frequencies and damping ratios of the sandwich microbeam

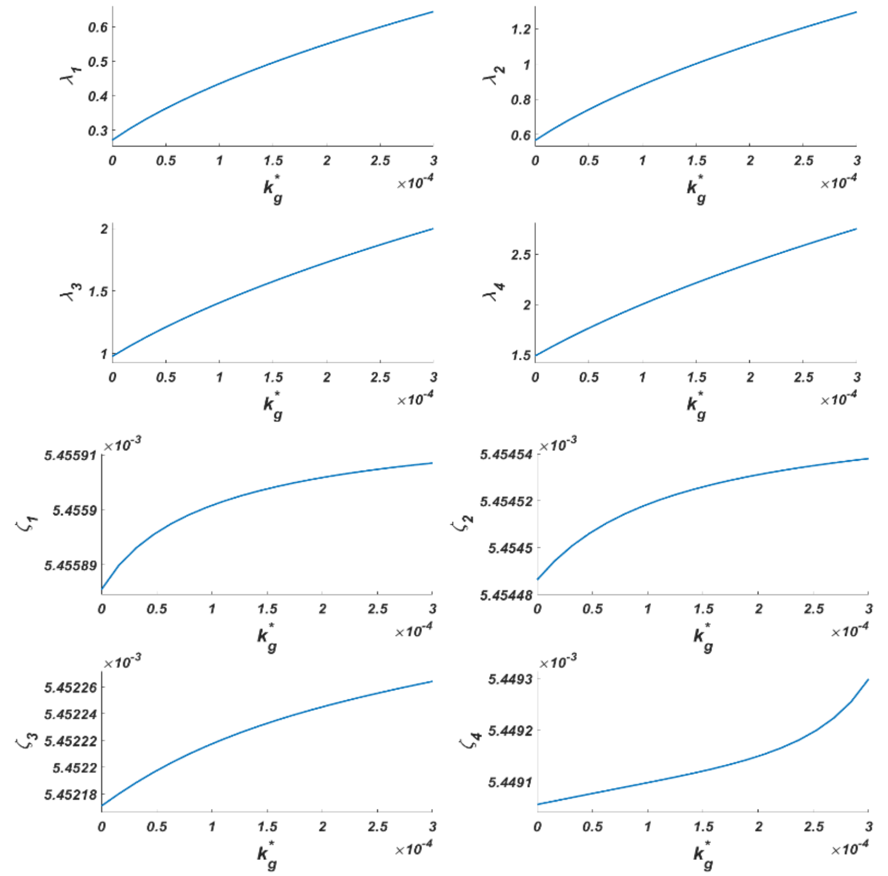

Figure 15. Effect of the foundation shear modulus on the natural frequencies and damping ratios

10.57647/jsm.2026.1801.03

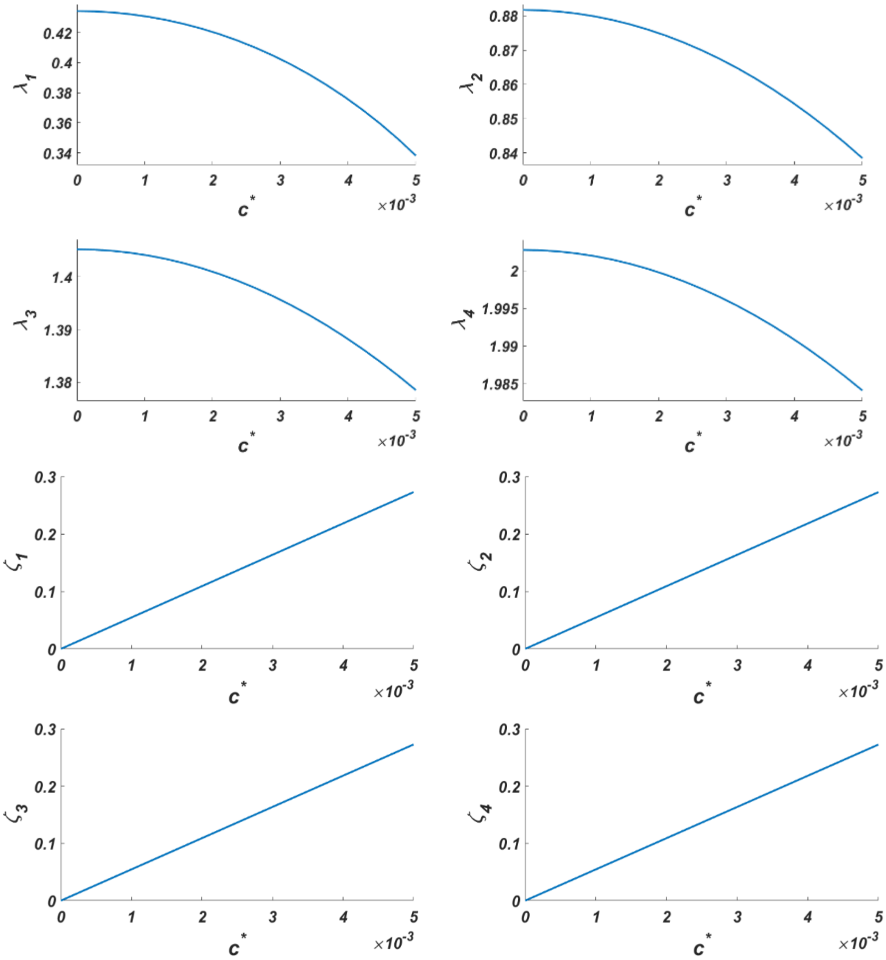

Figure 16. Effect of the foundation damping coefficient on the natural frequencies and damping ratios

7. Conclusion

In this study, the natural frequencies and damping ratios of the micro sandwich beam resting on a viscoelastic Winkler–Pasternak foundation are investigated for various edge conditions. MCST, Mori-Tanaka homogenization method, Gurtin-Murdoch model, and third-order shear deformation beam theory was used to derive the equations of motion.

The effect of surface inertia (Surface mass density) has been considered and the combination of the boundary conditions and motion equations have been solved by the DQM.

The main conclusions of the research may be listed as follows:

• An increase in the thickness of the viscoelastic porous core enhances energy dissipation, resulting in a uniform increase in damping coefficients.

• As the core porosity ratio increases, the natural frequencies and damping coefficients of the micro beam increase.

• An increase in the mass fraction of CNTs results in higher frequencies and an increase in the damping coefficients.

• To maximize the increase in natural frequencies, CNTs are distributed as close as possible to the top and bottom sheets of the micro beam.

• An increase in the material length scale parameter leads to greater stiffness and consequently higher natural frequencies of the micro beam.

• Normal and shear modulus significantly increase the dimensionless frequency of the sandwich beam, while the damping coefficient decreases it.

• Considering the density of surface effect has a slight impact on low frequencies but may be necessary for higher accuracy of the model at higher frequencies.

The practical implications of this study encompass the engineering of ultra-lightweight, high-damping sandwich microbeams for critical applications in aerospace (e.g., vibration-suppressing satellite panels), biomedical devices (e.g., implantable micro-sensors), and micro-electro-mechanical systems (MEMS/NEMS energy harvesters).

Acknowledge

The author would like to thank the reviewers for their comments and suggestions to improve the clarity of this article.

Authors Contribution
All the authors have participated sufficiently in the intellectual content, conception and design of this work or the analysis and interpretation of the data (when applicable), as well as the writing of the manuscript.

Availability of data and materials
The data that support the findings of this study are available from the corresponding author, upon reasonable request.

Conflict of interests
The author states that there is no conflict of interest.

References

[1] Liu, P., and Chen, G-F. 2014. Porous materials: processing andapplications: Elsevier.

[2] Gupta, N., Gupta, SM., and Sharma, S. 2019. Carbon nanotubes: synthesis, properties and engineering applications: *Carbon Letters* 29: 419-447. https://doi.org/10.1007/s42823-019-00068-2

[3] Babaei, M., Kiarasi, F., Asemi, K., et al. 2022. Functionally graded saturated porous structures: A review: *Journal of Computational Applied Mechanics* 53: 297-308. https://doi.org/10.22059/jcamech.2022.342710.719

[4] Enayat, S., Hashemian, M., Toghraie, D., et al. 2024. RETRACTED: Bending, buckling and vibration analyses of FG porous nanobeams resting on Pasternak foundation incorporating surface effects: *ZAMM-Journal of Applied Mathematics and Mechanics/Zeitschrift für Angewandte Mathematik und Mechanik* 104: e202000231. https://doi.org/10.1002/zamm.202000231

[5] Chen, D., Yang, J., and Kitipornchai, S. 2015. Elastic buckling and static bending of shear deformable functionally graded porous beam: *Composite Structures* 133: 54-61. https://dx.doi.org/10.1016/j.compstruct.2015.07.052

[6] Chen, D., Yang, J., and Kitipornchai, S,. 2016b. Free and forced vibrations of shear deformable functionally graded porous beams: *International journal of mechanical sciences* 108: 14-22.

[7] Chen, D., Kitipornchai, S., and Yang, J. 2016a. Nonlinear free vibration of shear deformable sandwich beam with a functionally graded porous core: *Thin-Walled Structures* 107: 39-48.

[8] Chen, D., Gao, K., Yang, J., et al. 2023. Functionally graded porous structures: analyses, performances, and applications–a review: *Thin-Walled Structures* 191: 111046. https://doi.org/10.1016/j.tws.2023.111046

[9] Kitipornchai, S., Chen, D., and Yang, J. 2017. Free vibration and elastic buckling of functionally graded porous beams reinforced by graphene platelets. *Materials & Design* 116: 656-665.

[10] Wu, D., Liu, A., Huang, Y., et al. 2018. Dynamic analysis of functionally graded porous structures through finite element analysis: *Engineering Structures* 165: 287-301. https://doi.org/10.1016/j.engstruct.2018.03.023

[11] Alphonse, M., Raja, VB., Krishna, VG., et al. 2021. Mechanical behavior of sandwich structures with varying core material–A review. *Materials Today: Proceedings* 44: 3751-3759. https://doi.org/10.1016/j.matpr.2020.11.722

[12] Safari, M., Mohammadimehr, M., and Ashrafi, H. 2021. Free vibration of electro-magneto-thermo sandwich Timoshenko beam made of porous core and GPLRC: *Adv. Nano Res* 10: 115-128.

[13] Eftekhari, SA., and Toghraie, D. 2022. Vibration and dynamic analysis of a cantilever sandwich microbeam integrated with piezoelectric layers based on strain gradient theory and surface effects: *Applied Mathematics and Computation* 419: 126867. https://doi.org/10.1016/j.amc.2021.126867

[14] Ruocco, E., and Reddy, J. 2023. Analytical solutions of Reddy, Timoshenko and Bernoulli beam models: A comparative analysis: *European Journal of Mechanics-A/Solids* 99: 104953. https://doi.org/10.1016/j.euromechsol.2023.104953

[15] Biglari, H., Teymouri, H., and Shokouhi, A. 2024. Dynamic Response of Sandwich Beam with Flexible Porous Core Under Moving Mass: *Mechanics of Composite Materials* 60: 163-182. https://doi.org/10.1007/s11029-024-10181-7

[16] Asgari, M., Mohammadimehr, M., Arabzadeh-Ziari, M., et al. 2025. Static bending, vibration, and buckling responses of a sandwich beam composed of five layers considering honeycomb core and CNTRC with sma particles and temperature-dependent material properties using SSDT: *Mechanics of Advanced Composite Structures* 12: 153-168. https://doi.org/10.22075/macs.2024.33537.1622

[17] Khoshgoftar, MJ., Mehdianfar, P., Shabani, Y., et al. 2025. Vibration Characteristics of Carbon Nanotube-Reinforced Sandwich Nanobeams with Hybrid Cellular Core. *Vibration* 8: 14. https://doi.org/10.3390/vibration8020014

[18] Shahedi, S., and Mohammadimehr, M. 2020. Vibration analysis of rotating fully-bonded and delaminated sandwich beam with CNTRC face sheets and AL-foam flexible core in thermal and moisture environments: *Mechanics Based Design of Structures and Machines* 48(5): 584-614. https://doi.org/10.1080/15397734.2019.1646661

[19] Rostami, R., and Mohammadimehr, M. 2022. Vibration control of rotating sandwich cylindrical shell-reinforced nanocomposite face sheet and porous core integrated with functionally graded magneto-electro-elastic layers: *Engineering with Computers* 38(1): 87-100. https://doi.org/10.1007/s00366-020-01052-5

[20] Mohammadimehr, M. 2024. The effect of a nonlocal stress-strain elasticity theory on the vibration analysis of Timoshenko sandwich beam theory: *Advances in nano research*, 17(3): 275-284. https://doi.org/10.12989/anr.2024.17.3.275

[21] Subbaratnam, B. 2023. Dynamic Stability of Beam on Elastic Foundation Including Higher Transition Foundation: *Challenges in Foundation Engineering-Case Studies and Best Practices. IntechOpen.* https://doi.org/10.5772/intechopen.113009

[22] Magnucki, K., and Magnucka-Blandzi, E. 2024. Dynamic stability of a three-layer beam–generalisation of the sandwich structure theory: acta mechanica et automatica 18: 1-7. https://doi.org/10.2478/ama-2024-0001

[23] Adab, N., and Arefi, M. 2023. Vibrational behavior of truncated conical porous GPL-reinforced sandwich micro/nano-shells: Engineering with Computers 39: 419-443. https://doi.org/10.1007/s00366-021-01580-8

[24] Nikbakhsh, P., Mohammadimehr, M., and Bargozini, F. 2025. Vibration of a Sandwich Plate with FG Porous and Auxetic Cores and Piezo-Electro-Magnetic Face Sheets: Physical Mesomechanics 28(6): 851-869. https://doi.org/10.1134/s1029959924601933

[25] Hashempour, MH., Ghorbanpour Arani, A., Khoddami Maraghi, Z., et al. 2025. Supersonic flutter and vibration analyses of a functionally graded porous-nanocomposite sandwich microbeam: *Journal of Solid Mechanics* 2: 118.

[26] Sadd, MH. 2009. *Elasticity: theory, applications, and numerics*: Academic Press.

[27] Reddy, JN. 2017. *Energy principles and variational methods in applied mechanics*: John Wiley & Sons.

[28] Tornabene, F., Bacciocchi, M., Fantuzzi, N., et al. 2019. Multiscale approach for three-phase CNT/polymer/fiber laminated nanocomposite structures: *Polymer composites* 40: E102-E126. https://doi.org/10.1002/pc.24520

[29] Arani, A.G., Maraghi, Z.K., and Arani, H.K., 2016. Orthotropic patterns of Pasternak foundation in smart vibration analysis of magnetostrictive nanoplate. Proceedings of the Institution of Mechanical Engineers, Part C: *Journal of Mechanical Engineering Science*, 230(4), pp.559-572. https://doi.org/10.1177/0954406215579929

[30] Arabloo Faraji, MJ, Ghorbanpour, Arani, A., Mamnoun, E., et al. 2025. Vibration analysis of sandwich beams with magnetorheological elastomer core and FGM graphene nanoplatelet-reinforced polymer faces on viscoelastic foundation: *Mechanics of Advanced Composite Structures* 12: 447-464. https://doi.org/10.22075/macs.2025.34687.1695

[31] Motallebi, MA., Hashemian, M., Eftekhari, SA., et al. 2025. Size-dependent flutter analysis of a nanobeam made of metal-ceramic functionally graded materials subjected to supersonic fluid flow: *Propulsion and Power Research* 14: 110-132. https://doi.org/10.1016/j.jppr.2025.02.008

[32] Gurtin, ME., and Ian, Murdoch, A. 1975. A continuum theory of elastic material surfaces: *Archive for rational mechanics and analysis* 57: 291-323. https://doi.org/10.1007/bf00261375

[33] Lu, P., He, L., Lee, H., et al. 2006. Thin plate theory including surface effects: *International Journal of Solids and Structures* 43: 4631-4647. https://doi.org/10.1016/j.ijsolstr.2005.07.036

[34] Liu, C., and Rajapakse, R. 2009. Continuum models incorporating surface energy for static and dynamic response of nanoscale beams: *IEEE Transactions on Nanotechnology* 9: 422-431.

https://doi.org/10.1109/tnano.2009.2034142

[35] Şimşek ,M.,and Reddy, J. 2013. A unified higher order beam theory for buckling of a functionally graded microbeam embedded in elastic medium using modified couple stress theory: *Composite Structures* 101: 47-58. https://doi.org/10.1016/j.compstruct.2013.01.017

[36] Khani, Arani, H., Shariyat, M., and Mohammadian, A. 2020. Vibration analysis of magnetostrictive nano-plate by using modified couple stress and nonlocal elasticity theories: *Int J Mater Metall Eng* 14: 229-234.

[37] Arani, HK., and Shariyat, M. 2023. Nonlinear 2D-DQ volume-preservative global–local dynamic analysis of composite sandwich plates with soft hyperelastic cores and viscoelastic Winkler-Pasternak foundations: *Structures. Elsevier* 727-746. https://doi.org/10.1016/j.istruc.2023.06.057

[38] Arani ,HK., and Shariyat, M. 2022. Nonlinear Dynamic Response of an Abruptly Loaded Rubber-Like Hyperelastic Plate Resting on a Dissipative Viscoelastic Winkler–Pasternak Medium: *Iranian Journal of Science and Technology, Transactions of Mechanical Engineering* 1-18. https://doi.org/10.1007/s40997-022-00512-1

[39] Shu, C. 2012. Differential quadrature and its application in engineering: Springer Science & Business Media.

[40] Mohammadimehr, M., and Mehrabi. M. 2017. Stability and free vibration analyses of double-bonded micro composite sandwich cylindrical shells conveying fluid flow: *Applied Mathematical Modelling* 47: 685-709. https://doi.org/10.1016/j.apm.2017.03.054

[41] Arani, AG., Maraghi, ZK., and Arani, HK. 2016. Smart vibration control of magnetostrictive nano-plate using nonlocal continuum theory*: Journal of Solid Mechanics* 8: 300-314. https://doi.org/10.1177/1077546315588222